The Formation of Terraces on Asteroid (101955) Bennu

O. S. Barnouin, M. G. Daly, J. A. Seabrook, Y. Zhang, F. Thuillet, P. Michel, J. H. Roberts, R. T. Daly, M. E. Perry, H. C. M. Susorney, et al.

▶ **To cite this version:**

O. S. Barnouin, M. G. Daly, J. A. Seabrook, Y. Zhang, F. Thuillet, et al.. The Formation of Terraces on Asteroid (101955) Bennu. Journal of Geophysical Research. Planets, 2022, 127, 10.1029/2021JE006927 . insu-03656900

HAL Id: insu-03656900
https://insu.hal.science/insu-03656900

Submitted on 2 May 2022

HAL is a multi-disciplinary open access archive for the deposit and dissemination of scientific research documents, whether they are published or not. The documents may come from teaching and research institutions in France or abroad, or from public or private research centers.

L'archive ouverte pluridisciplinaire **HAL**, est destinée au dépôt et à la diffusion de documents scientifiques de niveau recherche, publiés ou non, émanant des établissements d'enseignement et de recherche français ou étrangers, des laboratoires publics ou privés.

Distributed under a Creative Commons Attribution 4.0 International License

Check for updates

JGR Planets

RESEARCH ARTICLE
10.1029/2021JE006927

The Formation of Terraces on Asteroid (101955) Bennu

O. S. Barnouin[1], M. G. Daly[2], J. A. Seabrook[2], Y. Zhang[3], F. Thuillet[3], P. Michel[3], J. H. Roberts[1], R. T. Daly[1], M. E. Perry[1], H. C. M. Susorney[4], E. R. Jawin[5], R.-L. Ballouz[6], K. J. Walsh[7], M. M. Sevalia[8], M. M. Al Asad[4], C. L. Johnson[4,9], E. B. Bierhaus[10], R. W. Gaskell[9], E. E. Palmer[9], J. Weirich[9], B. Rizk[6], C. Y. Drouet D'Aubigny[6], M. C. Nolan[6], D. N. DellaGiustina[6], D. J. Scheeres[11], J. W. McMahon[11], H. C. Connolly Jr.[6,12], D. C. Richardson[13], C. W. V. Wolner[6], and D. S. Lauretta[6]

[1]The Johns Hopkins University Applied Physics Laboratory, Laurel, MD, USA, [2]The Centre for Research in Earth and Space Science, York University, Toronto, ON, Canada, [3]Observatoire de la Côte d'Azur, CNRS, Laboratoire Lagrange, Université Côte d'Azur, Nice, France, [4]The University of British Columbia, Vancouver, BC, Canada, [5]Smithsonian National Museum of Natural History, Washington, DC, USA, [6]Lunar and Planetary Laboratory, University of Arizona, Tucson, AZ, USA, [7]Southwest Research Institute, Boulder, CO, USA, [8]Mount Hebron High School, Ellicott City, MD, USA, [9]Planetary Science Institute, Tucson, AZ, USA, [10]Lockheed Martin Space, Littleton, CO, USA, [11]Smead Department of Aerospace Engineering Sciences, University of Colorado, Boulder, CO, USA, [12]Department of Geology, Rowan University, Glassboro, NJ, USA, [13]Department of Astronomy, University of Maryland, College Park, MD, USA

Abstract The surface of the rubble-pile asteroid (101955) Bennu has been characterized in detail by the OSIRIS-REx (Origins, Spectral Interpretation, Resource Identification, and Security–Regolith Explorer) mission. By examining global and local digital terrain models, we observed that Bennu possesses terraces, that is, a series of roughly latitude-parallel, step-like slope breaks. These partially circumscribe the poles and extend east-west over several longitudinal quadrants at mid- to high (≥30°) latitudes. The terraces are subtle in amplitude, with heights ranging from 1 to 5 m. They often exhibit back-wasting that results in V-shaped scarps that open downslope in some locations. When boulders >5–10 m are absent at or near a terrace, the steeper portion (the drop) of the terrace lacks rocks, whereas the flatter portion (the bench) of the terrace has accumulations of rocks at its crest. When boulders >5–10 m are present, their steep downslope faces often make up the drop from the terrace crest, and they retain debris upslope, thereby enhancing the terrace structure. A geotechnical stability analysis indicates that Bennu's surface is likely unstable and that surface cohesion is <0.6 Pa. Bennu's terraces strongly resemble scarps generated in laboratory and numerical simulations of a cohesionless granular bed as the slope of the bed increases quasi-statically. We conclude that terraces are probably actively forming on Bennu as its surface slowly fails owing to creep induced by spin acceleration.

Plain Language Summary Analyzing the landscape of a planetary body can shed light on the processes that shape its surface over time. We used data acquired by the OSIRIS-REx (Origins, Spectral Interpretation, Resource Identification, and Security–Regolith Explorer) mission to explore the rubble-covered landscape of the near-Earth asteroid Bennu. We observed subtle step-like features, or terraces, no more than about 5 m in relief (about half the height of a telephone pole). These terraces are approximately parallel to lines of latitude (i.e., they run east–west) and are located in both the northern and southern hemispheres of Bennu, but not near the equator. Accumulations of rocks tend to be present at the terrace crests, and the terrace faces are usually smooth. Boulders 5–10 m in size form some terraces and enhance the terrace structure by retaining loose material upslope. Laboratory experiments and numerical simulations show that subtle terraces can form in Bennu-like conditions if the slope of the surface increases. Thus, these landforms are evidence for the ongoing "creep" of loose material on Bennu as surface slopes change in response to the gradual acceleration in the asteroid's spin rate.

Key Points:

- Bennu exhibits subtle latitudinal terracing at mid- to high latitudes
- Terrace surface expressions follow expectations from laboratory and numerical investigations
- Terraces are an expression of Bennu's current surface instability

Correspondence to:

O. S. Barnouin,
olivier.barnouin@jhuapl.edu

Citation:

Barnouin, O. S., Daly, M. G., Seabrook, J. A., Zhang, Y., Thuillet, F., Michel, P., et al. (2022). The formation of terraces on asteroid (101955) Bennu. *Journal of Geophysical Research: Planets*, *127*, e2021JE006927. https://doi.org/10.1029/2021JE006927

Received 16 APR 2021
Accepted 18 NOV 2021

Author Contributions:

Conceptualization: R. T. Daly, E. R. Jawin, R.-L. Ballouz, K. J. Walsh, C. L. Johnson, E. B. Bierhaus, D. S. Lauretta
Data curation: J. A. Seabrook, B. Rizk, C. Y. Drouet D'Aubigny, D. N. DellaGiustina, D. J. Scheeres, J. W. McMahon
Formal analysis: J. A. Seabrook, J. H. Roberts
Funding acquisition: E. B. Bierhaus, D. S. Lauretta
Investigation: Y. Zhang, F. Thuillet, J. H. Roberts, R. T. Daly, M. E. Perry, H. C. M. Susorney, E. R. Jawin, R.-L. Ballouz, K. J. Walsh, M. M. Sevalia, M. M. Al Asad, E. B. Bierhaus, M. C. Nolan, D. N. DellaGiustina, D. J. Scheeres, J. W. McMahon, H. C. Connolly, C. W. V. Wolner, D. S. Lauretta
Methodology: Y. Zhang, F. Thuillet, J. H. Roberts, R. T. Daly, E. R. Jawin, M. M. Al Asad, C. L. Johnson, E. B. Bierhaus, R. W. Gaskell, E. E. Palmer, J. Weirich, B. Rizk, M. C. Nolan, H. C. Connolly, C. W. V. Wolner

© 2022. The Authors.
This is an open access article under the terms of the Creative Commons Attribution License, which permits use, distribution and reproduction in any medium, provided the original work is properly cited.

1. Introduction

The Origins, Spectral Interpretation, Resource Identification, and Security-Regolith Explorer (OSIRIS-REx) spacecraft arrived at (101955) Bennu in late 2018 (Lauretta, DellaGiustina, et al., 2019). Images and laser altimetry observations have enabled the construction of global digital terrain models (GDTMs; Barnouin et al., 2020) of the asteroid. Bennu is a top-shaped, rubble-pile asteroid (Barnouin et al., 2019) made from reaccumulated

Project Administration: D. S. Lauretta
Resources: E. R. Jawin, K. J. Walsh, C. L. Johnson, B. Rizk, C. Y. Drouet D'Aubigny, M. C. Nolan, D. N. DellaGiustina, D. J. Scheeres, J. W. McMahon, H. C. Connolly, C. W. V. Wolner
Software: J. A. Seabrook, Y. Zhang, F. Thuillet, R. W. Gaskell, E. E. Palmer, J. Weirich, D. C. Richardson
Supervision: C. L. Johnson, M. C. Nolan, D. N. DellaGiustina, H. C. Connolly, C. W. V. Wolner, D. S. Lauretta
Visualization: Y. Zhang, F. Thuillet, M. M. Sevalia, B. Rizk, C. Y. Drouet D'Aubigny, D. N. DellaGiustina, C. W. V. Wolner
Writing – original draft: Y. Zhang, F. Thuillet, J. H. Roberts, R. T. Daly, M. E. Perry, D. S. Lauretta
Writing – review & editing: Y. Zhang, J. H. Roberts, R. T. Daly, M. E. Perry, C. L. Johnson, C. W. V. Wolner, D. S. Lauretta

fragments of a larger parent body that was catastrophically disrupted. Loose surface material (regolith) on this asteroid migrates from the high and mid-latitudes toward the equator (M. G. Daly et al., 2020; Jawin et al., 2020). An initial assessment of the first reliable GDTM of Bennu created by the OSIRIS-REx mission, which considered measurements of surface slope (Scheeres et al., 2019) and elevation relative to gravity, indicated that Bennu likely possesses some interior stiffness (Barnouin et al., 2019). The evidence for such stiffness includes long surface lineaments such as grooves seen across the asteroid (Barnouin et al., 2019). Such features cannot easily form in an unconsolidated asteroid, where significant seismic attenuation is expected (e.g., J. E. Richardson et al., 2005), unless a connectivity exists within Bennu's rubble that allows stresses to propagate and generate cracks (e.g., Marchi et al., 2015; Thomas et al., 2002).

Additional indicators of subsurface stiffness on Bennu include: (a) The presence of longitudinal ridges, not yet observed on other top-shaped asteroids, that extend from pole to pole. These broad regions possess greater elevations and are eroding more slowly than the surrounding terrain (Barnouin et al., 2019; M. G. Daly et al., 2020). (b) A landslide deposit, filling a large mid-equator crater located at 8°N and 269°E; and other regional evidence for mass movements (Jawin et al., 2020). Bennu is experiencing rotational acceleration (spin-up) due to thermally driven torques known as the Yarkovsky-O'Keefe-Radzievskii-Paddack (YORP; Rubincam, 2000) effect (Hergenrother et al., 2019; Nolan et al., 2019); numerical investigations of the YORP effect indicate that the observed mass wasting occurs preferentially on the surface of top-shaped asteroids when the asteroid interior is too stiff to allow deep-seated failures to accommodate any stress build-up (Walsh et al., 2008; Zhang et al., 2018). (c) The presence of mound craters, and shallow depth-to-diameter ratios of large (>50 m) craters, indicating a subsurface layer with some strength (R. T. Daly et al., 2020) may exist at 3–10 m depth.

The effects of the surface displacement and re-adjustment on Bennu also manifest as hemispherical shape differences (M. G. Daly et al., 2020). The southern ($-Z$) hemisphere of Bennu has a radius of curvature that is smaller (rounder) than its northern ($+Z$) counterpart. The greater roundness of the southern hemisphere probably results from accumulations of unconsolidated regolith retained by very large (>30 m diameter) boulders and the shallower slopes that delineate this hemisphere's perimeter (M. G. Daly et al., 2020). Images show that up to 10 m of material has accumulated onto and flowed around some of these large boulders (Jawin et al., 2020). In the north, such large retaining boulders are uncommon, and evidence for more substantial mass movement exists, especially between the longitudinal ridges (M. G. Daly et al., 2020). In both the north and south, some of the boulders appear to have re-orientated with their long-axis in a N-S, downslope direction (Schwartz et al., 2019), consistent with a surface that is creeping over time. Such creeping changes are expected given the gradual YORP-driven increase in Bennu's spin rate of $3.63 \pm 0.52 \times 10^{-6\circ}$ day^{-2} (current spin period ≈ 4.3 hr; Hergenrother et al., 2019).

Here we present observations of another morphological aspect of Bennu's surface: terraces, or a series of roughly latitude-parallel (east-west), step-like slope breaks that circumscribe the poles. To explore the geological characteristics of these landforms, we use high-resolution DTMs constructed from data obtained by the OSIRIS-REx Laser Altimeter (OLA; Barnouin et al., 2020; M. G. Daly et al., 2017; Seabrook et al., 2019) and surface images acquired by the OSIRIS-REx Camera Suite (OCAMS; Golish et al., 2020; Rizk et al., 2018). We present simple slope stability assessments (Iverson et al., 1997) to explore whether slowly evolving slope changes due to the measured spin-up of Bennu (Hergenrother et al., 2019; Nolan et al., 2019) can lead to slope failure. We supplement these geotechnical assessments with laboratory and numerical investigations to understand the mechanics and surface expressions of surface failure that spin-up might cause in a micro-gravity environment and compare these expressions to the terraces observed on Bennu. We use our results to further our understanding of Bennu's surface properties and evolution.

2. Observations

We used the OSIRIS-REx Laser Altimeter (OLA) v20 GDTM and local digital terrain models (LDTMs; M. G. Daly et al., 2020), all of which are accurate to <0.15 m radially, to identify and characterize terraces at global and regional scales. The GDTM samples the surface of Bennu with a ground sample distance (GSD) of ~0.8 m, whereas the LDTMs does so at 0.05 m GSD, equal to about the size of the OLA footprint. The properties of the terraces were assessed using slope and elevation data overlain on the DTMs. Here, slope is computed as the angle between the surface normal from individual polyhedral facets and the local gravity field (e.g., Scheeres et al., 2016). Elevation is the difference between the local gravitational potential at the surface and a reference

potential (geoid), divided by the local acceleration due to gravity where rotational effects are included (e.g., Barnouin et al., 2019; Barnouin-Jha et al., 2008; Cheng et al., 2002; Scheeres et al., 2016, 2019).

2.1. Global Evidence

In polar views of Bennu, we observed steep slopes (>30°; Figure 1 white arrows), followed by flattening (<20°) as one moves downslope from pole to equator. These scarp- or step-like breaks in slope appear to surround the pole along lines of latitudes.

Global assessments of slope and elevation (Figure 2) provided additional evidence for the near-circumferential or latitudinally aligned nature of these breaks in slopes. They are visible at latitudes poleward of 30° and −30° and can extend between longitudinal quadrants, sometimes drifting in latitude, as evident from the polar views (Figure 2). When we linearly detrended elevation by removing a linear slope fit for elevations above 20° and below −20° of latitude, the crests of the slope breaks became more apparent. The crests are more regular in amplitude and spacing in the N–S direction and span broader E–W extents in the southern hemisphere when compared to the north, and they are one of the indicators of hemispherical differences discussed in M. G. Daly et al. (2020). The regularity in spacing and extent create a step-like appearance when the asteroid is viewed from the poles.

On the basis of this global evidence, we classified the step-like features as terraces. The terraces are preferentially evident between latitudes of 35° and 65° where the global slopes on Bennu reach maximum values (Scheeres et al., 2019). Thus, they might be the product of localized slope failure.

2.2. Regional Evidence

In detailed regional assessments of Bennu (Figure 3), we found that as one moves downslope from Bennu's pole to its equator, the terraces observed in the global views are often the result of accumulations of larger boulders at or near a local crest on a flatter bench. The crest is followed by a steep drop downslope, which eventually flattens to the next bench, whose crest again exhibits an accumulation of material, thereby producing the next terrace structure. Often, the steep drop consists of the boulder walls that comprise the terrace crest. Where the steep drop does not consist of ≥5 m boulder face, images show a fairly smooth surface lacking in smaller boulders and rocks (Figure 4).

The terraces on Bennu are topographically subtle, with typical amplitudes of 1–5 m (Figures 2 and 5). They are identified fairly readily as latitudinal structures in the GDTM where the topography is averaged over GSDs of 0.8 m (Figure 5c). But the numerous rocks and boulders across Bennu at the meter scale, as apparent in LDTMs with GSDs of 0.2 m (Figures 5d and 5e), seem to obscure the terraces, mainly because of the many peaks and valleys created by these objects. These rocks are essentially high-frequency noise. But after detrending profiles across this and other areas of Bennu (Figures 3 and 6) by removing regional slopes, we observe that broad but shallow variations in surface height remain, confirming the presence of terraces.

Although the terrace heights of a few meters may appear minor in a terrestrial context, they are significant for Bennu. Given that the total elevation change on Bennu is ∼85 m (Barnouin et al., 2019), height changes observed at terraces range from 1% to 6% of the dynamic range of Bennu's topography. These terraces would represent height changes of 300–1,500 m on Earth.

The 0.2-m-GSD LDTMs (T1–T5 in Figures 3, 5, and 6) show that the E–W extent of some of the terraces are more complex in nature and more often interrupted than might be expected from the lower-resolution, smoother views of the 0.8-m-GSD GDTM. These terraces undulate along lines of latitude when analyzed in detail in the LDTMs. And in some instances, candidate impact craters (circular depressions) influence the E–W extent of the terraces (see Figures 3 and 6). Further, V-shaped depressions are present that open downslope and occasionally expand to become wide (>10 m from wall-to-wall) but short (<50 m downstream) troughs (e.g., Figure 5). These depressions occur at random along some terraces possibly because of localized zones of weakness caused by the mix of large and small particle sizes that exist on Bennu's surface (Barnouin et al., 2019; Lauretta, DellaGiustina, et al., 2019; Scheeres et al., 2019). The greater regularity in amplitude and E–W extent of the terraces in the southern hemisphere (Figure 2) suggests that the surface material there has a particle-size distribution and thickness

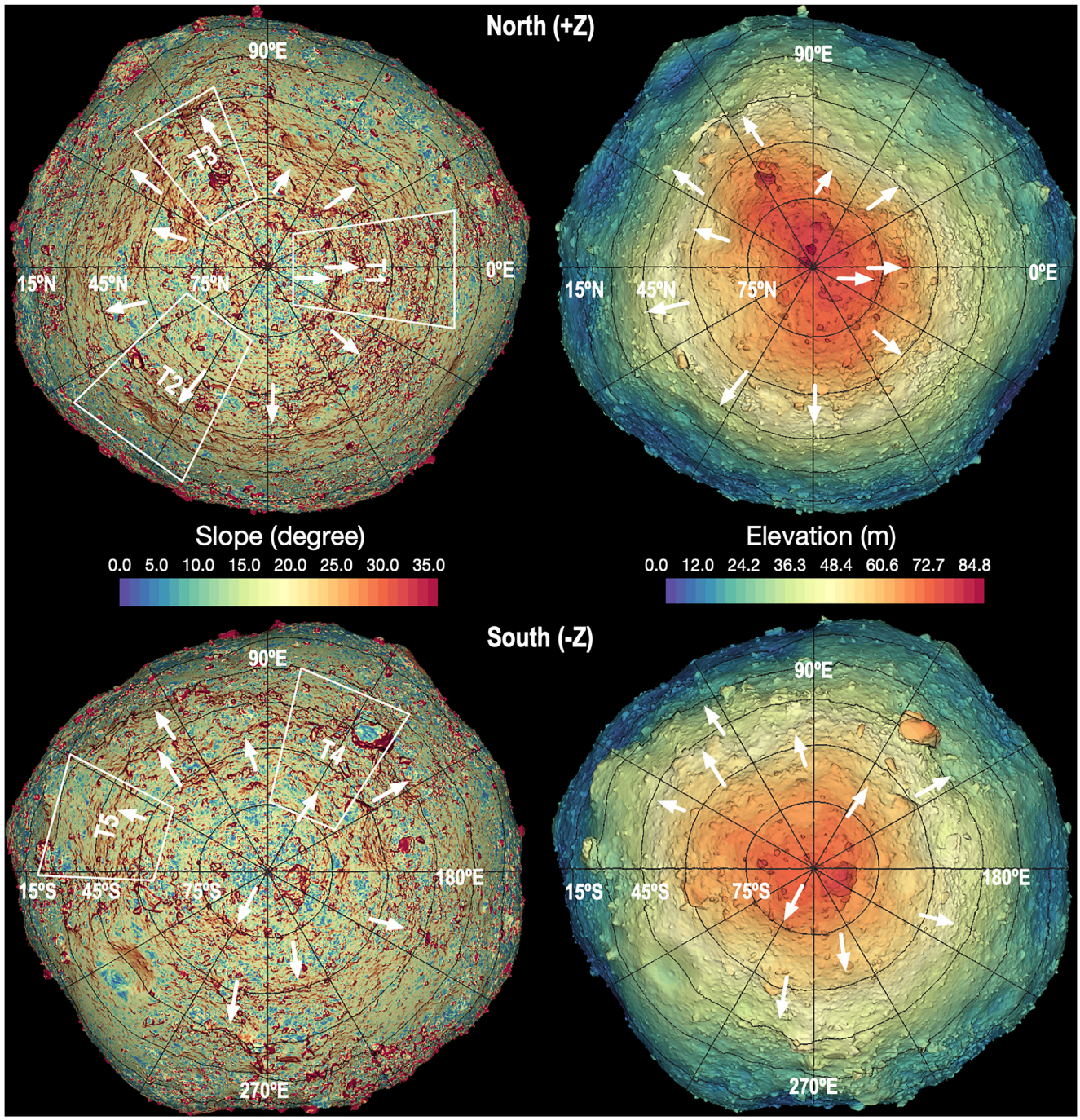

Figure 1. Evidence for terracing on Bennu circumscribing Bennu's pole. The model presented is derived from OSIRIS-REx laser altimetry data (OLA GDTM v20) and processed as described in (M. G. Daly et al., 2020). IDs T1, T2, and so on with corresponding white outlines indicate areas selected for regional studies. Arrows indicate the locations of terraces.

that do not vary much. Surface roughness at 0.1 and 0.3 m horizontal baselines (M. G. Daly et al., 2020) indicates that the smoother southern hemisphere has smaller particles on average (probably because of the presence of large boulders that act to retain these particles). In the north, there is greater variability in the location and E-W extent of the terraces, which is a consequence of the broader particle-size distribution of surface material present in the north relative to the south, leading to a greater measured surface roughness (M. G. Daly et al., 2020).

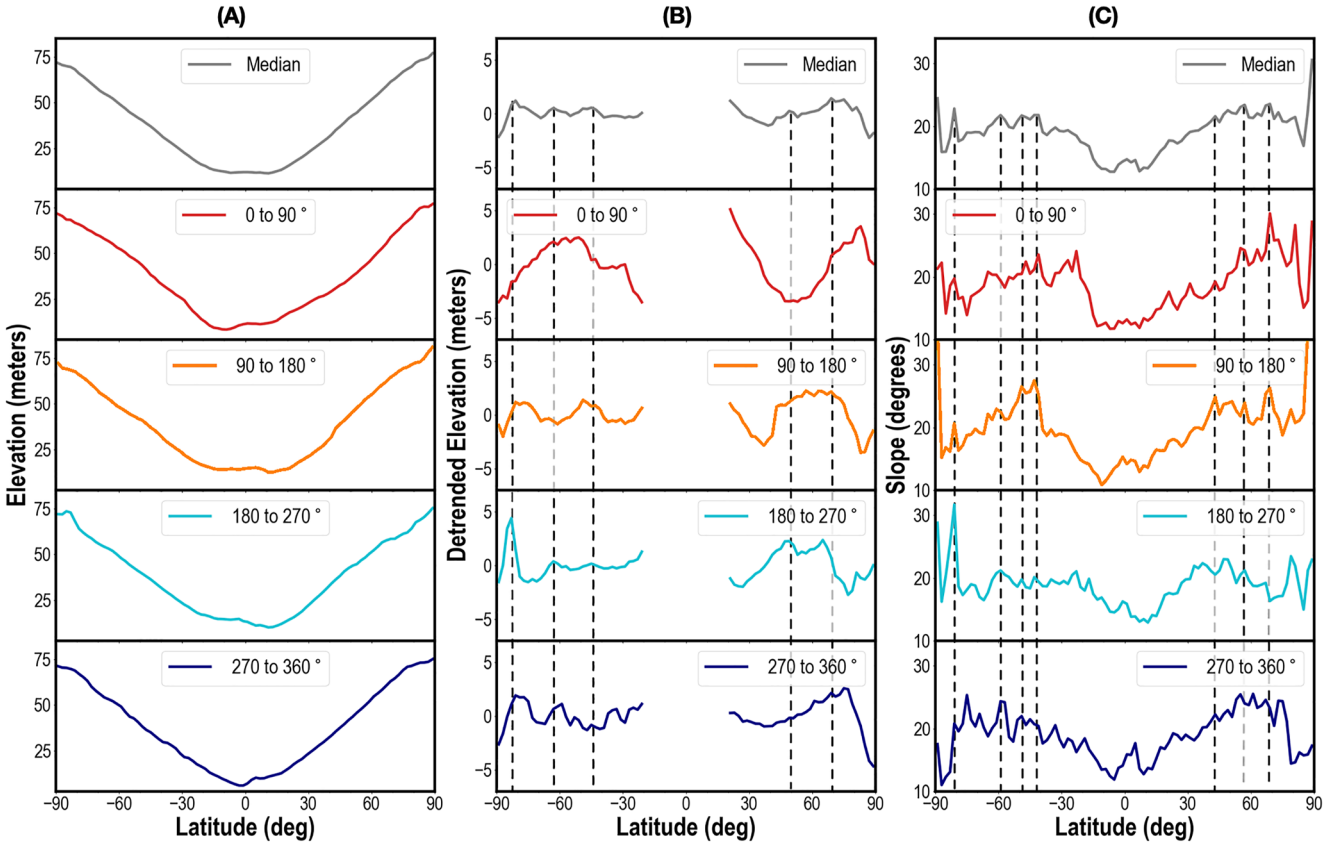

Figure 2. (a) Global and regional elevation, (b) detrended elevation, and (c) slope as a function of latitude on Bennu. The top plot in each panel shows a median profile for the entire asteroid, while the four lower plots show median profiles over four longitudinal quadrants from longitudes of 0°–90°, 90°–180°, 180°–270°, and 270°–360°. The detrended data (b) are obtained by first fitting a linear function to the median elevation above 20° in (a) as a function of latitude, then subtracting this fit from the observation. Black dotted lines denote crests that are frequently present in two or more longitudinal quadrants. Light gray dotted lines indicate a quadrant where a crest is not visible.

2.3. Boulders

Some terraces co-occur with the large boulder sizes that have been associated with the retention of particulate material (M. G. Daly et al., 2020). Figure 7 shows a clear step in the topography in the vicinity of a 25-m-diameter boulder that extends well beyond its W and E edges. This boulder contributes significantly to the regional terrace by effectively holding back both large and small debris and reducing regional downslope motion. This retention is evidenced by rocks and additional boulders accumulating on the upslope side of the large central boulder (see sideview of the LDTM in Figure 7), and burial via embayment especially around it. On the downslope side of this terrace (visible in the upslope view of Figure 7), and other boulder-dominated terraces, many boulders appear perched and undercut, probably as a result of removal of material that has made its way downslope (M. G. Daly et al., 2020; Jawin et al., 2020).

3. Slope Stability Analysis

The observed geomorphology of the terraces is highly suggestive of localized slope failure along broad lateral regions of the asteroid, possibly as the result of some subtle, creeping process associated with the known spin-up occurring currently at Bennu (Hergenrother et al., 2019; Nolan et al., 2019). To determine whether slope failure is possible in the areas on Bennu where the terraces are formed, we performed a slope stability analysis used commonly in terrestrial environments called the "factor of safety" or FS for infinite slope (e.g., Iverson et al., 1997). Such an analysis is typically undertaken terrestrially as the first step in assessing whether a slope is prone to displacement due to its steepness (e.g., Iverson et al., 1997). This analysis assumes a failing layer is thin relative to the length (~85 m) of the regional slope. We consider this assumption suitable for our purposes given

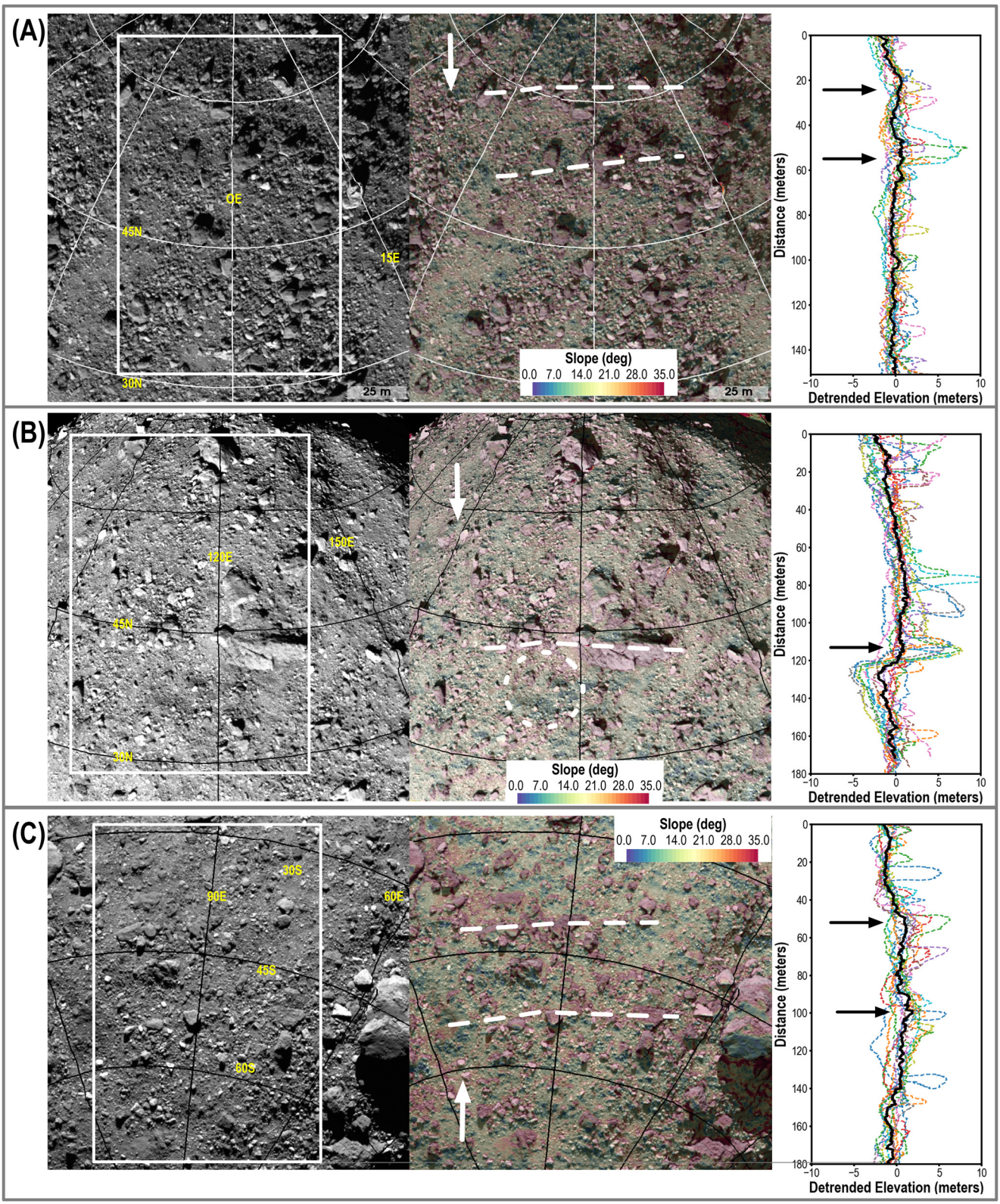
(A)
0E
45N
15E
30N
25 m
Slope (deg)
0.0 7.0 14.0 21.0 28.0 35.0
25 m
Distance (meters)
Detrended Elevation (meters)
(B)
120E
150E
45N
30N
Slope (deg)
0.0 7.0 14.0 21.0 28.0 35.0
Distance (meters)
Detrended Elevation (meters)
(C)
30S
90E
60E
45S
60S
Slope (deg)
0.0 7.0 14.0 21.0 28.0 35.0
Distance (meters)
Detrended Elevation (meters)

Figure 3.

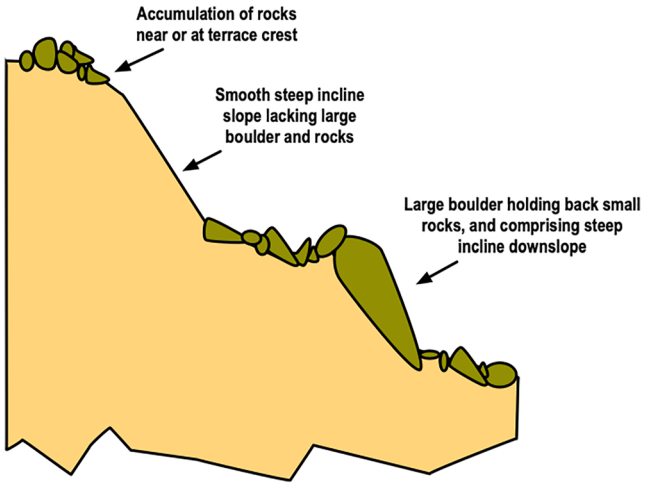

Figure 4. Side-view schematic highlighting the observed attributes of terraces on Bennu. Elevation changes shown are exaggerated relative to what is observed on the asteroid.

the aforementioned evidence (Section 1) that Bennu possesses $a \leq 10$ m loose layer on top of a stiffer interior. The ratio of resisting frictional and cohesive stresses to gravity is then given by:

$$FS = \frac{\tan\phi}{\tan\theta} + \frac{c}{\gamma_t T \sin\phi} \quad (1)$$

where θ is the slope angle, ϕ is the frictional angle of the surface material, c is the cohesion, γ_t is the depth-averaged total unit weight (layer bulk density times the local acceleration due to gravity), and T is the thickness of the unconsolidated surface layer (mixture of boulders and regolith) that could fail. Values of $FS < 1$ imply the slope is prone to failure. We used the lowest-resolution OLA GDTM available (average facet size of 12.5 m) for this analysis to minimize local slope biases in our assessment from individual boulders. We first considered cohesionless cases with ϕ spanning from 28° to 40° to simulate rounded to angular granular materials (essentially rounded cobbles to angular talus). Based on our assessment of Bennu images, most boulders are sub-angular to angular talus materials (DellaGiustina et al., 2021) and are more likely to have ϕ values >34°.

We also explore the effects of cohesion, c. Recall that a global cohesion value of $c = 1$ Pa is sufficient to form the equatorial ridge of Bennu (Roberts et al., 2021; Scheeres et al., 2019). As a endmember case (Figure 8), we use $c = 1$ Pa with the plausible $\phi = 40°$ and $T = 3$ m. This thickness is derived from the depths of mounds at the centers of three craters on Bennu (R. T. Daly et al., 2020), which offer one direct measure of the approximate depth of the unconsolidated surface layer (Quaide & Oberbeck, 1968). But geomorphic assessments of mass movement (Jawin et al., 2020; Perry et al., 2022) elsewhere on Bennu indicate that surface debris with thicknesses of up to 10 m are readily mobilized. We therefore consider lower values of $c \geq 0.1$ for a broader range of plausible surface debris thicknesses (Figure 9), with $\phi = 34°$ and 40°.

The results (Figure 8) indicate that for cohesionless conditions, Bennu's surface is failing currently, even in areas that are not near the downslope faces of large boulders. A decrease in ϕ, or equivalently, a slight increase in Bennu's spin rate that increases the slope angle, would make larger portions of the asteroid surface unstable. The *FS* analysis also indicates that failure occurs locally, and not generally across the whole asteroid. Local slopes stabilize after failing, but nearby, steeper areas are prone to fail as the asteroid's spin rate accelerates, leading to ongoing surface creep. Eventually, surface creep will no longer be able to stabilize the surface as slopes continue to increase, and global mass wasting—where large swaths of Bennu's surface fail under their own weight—should take place. However, we infer that this has not occurred recently given the presence of an old equatorial ridge (Walsh et al., 2019). According to the *FS* analysis, the regions of current failure are primarily above 30° of latitude in both the northern and southern hemispheres. These areas are where evidence for surface flows (Barnouin et al., 2019; M. G. Daly et al., 2020; Jawin et al., 2020; Perry et al., 2022; Walsh et al., 2019) and the terraces described here are observed.

Figure 8 also shows that $c = 1$ Pa completely suppresses all flow across the entire asteroid for $T = 3$ m. More specifically, Figure 9 indicates that only ≥0.2 Pa would be sufficient to globally suppress surface mobility at this thickness (Figure 9), and a value of ≈0.6 Pa prevents motion for $T = 10$ m (maximum flow thickness permissible based on current observations; Jawin et al., 2020). However, such suppression of surface motion is inconsistent with the evidence for surface flow that this and other studies find (e.g., M. G. Daly et al., 2020; Jawin et al., 2020; Walsh et al., 2019). Therefore, the presence of cohesion in excess of 0.6 Pa in the top few meters of Bennu's

Figure 3. (a) Terraces T1, (b) T3, and (c) T4 illustrate the regional attributes of these landforms. Locations are shown in Figure 1. The left column shows OSIRIS-REx Camera Suite (OCAMS) images collected on 18 April 2019 at (a) 19:12:26 UTC, (b)18:15:52 UTC, and (c) 19:57:15 UTC, respectively, and draped over an OLA GDTM (v20) with a ground sample distance of 0.8 m. The middle column shows slope draped on the GDTM and the OCAMS image, with arrows indicating overall downward slope direction, and dashed lines showing terrace crests. The right column shows 12–16 individual profiles (color), plus their median (black) taken through the square region outlined in the left column. The profiles are evenly spaced across the square region. Each profile was detrended by first fitting a linear function to the elevation with distance along the surface, and then subtracting this fit from the data, before the median is applied, to highlight regional terrace crests (arrows).

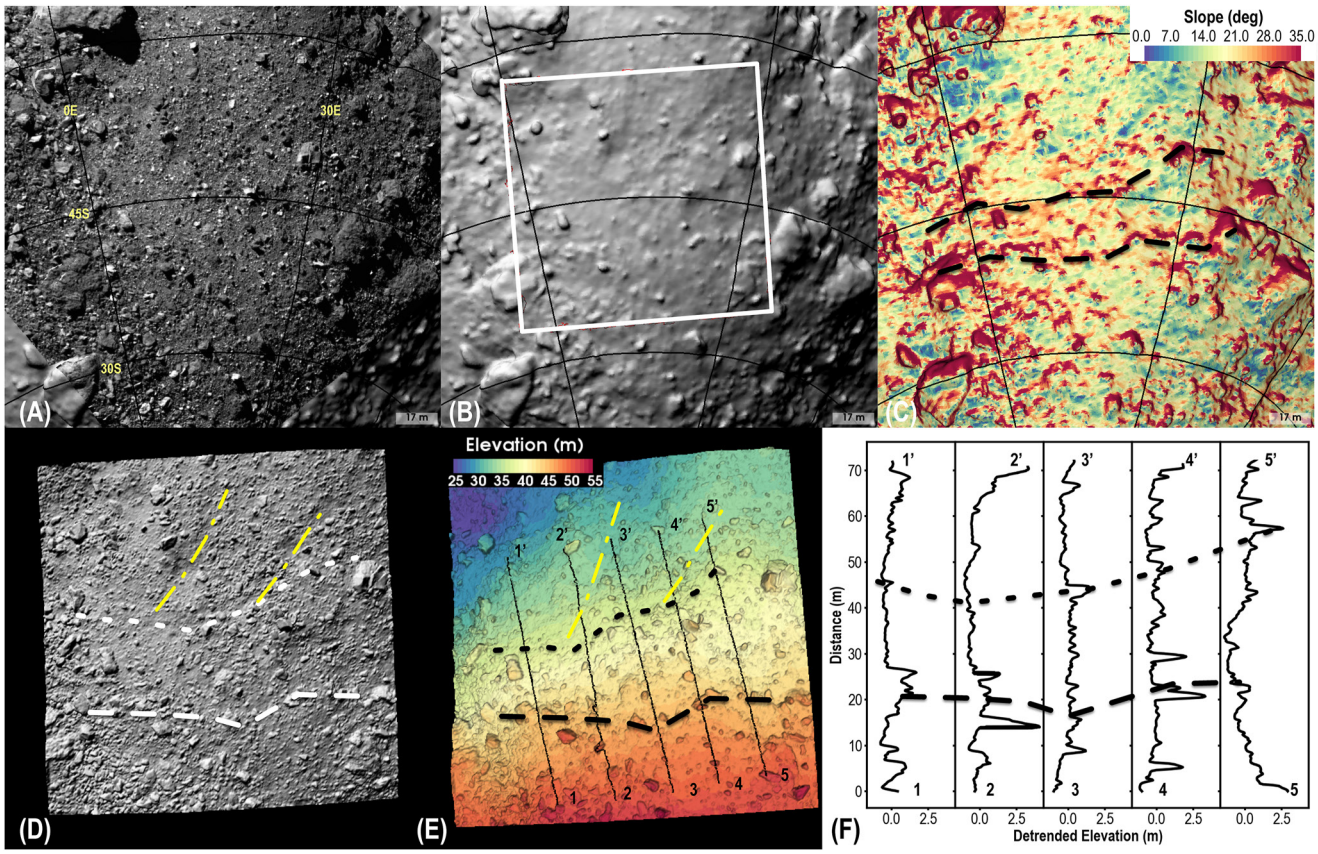

Figure 5. (a) Detailed view of region T5 in Figure 1 in an OSIRIS-REx Camera Suite image obtained on 27 May 2019 at 10:58:26 UTC and (b) a zoom-in on the OLA v20 GDTM with a ground sample distance (GSD) of 0.80 m. The GDTM is colored by slope in (c). The outline in (b) shows the location of the higher-resolution local digital terrain model with 0.20 m GSD shown in (d) and colored by elevation in (e). Profiles across two terraces (dashed lines) are identified in (e) and are shown in (f), after the regional slope has been removed from each by fitting and subtracting a linear function fit to the elevation with distance to highlight the undulations in the topography associated with the terraces indicated by the dashed lines in (c, d, and f), respectively. The yellow diagonal dash-dot-dash line in (d and f) indicate troughs that start as V-shaped mass-wasting regions initiating in the terraces.

surface material seems unlikely, although there is evidence for stiffness and strength at depth (e.g., Barnouin et al., 2019; R. T. Daly et al., 2020).

4. Assessing the Dynamics of Surface Failure During Spin-Up

To determine whether the terraces on Bennu are the result of creep-like failure processes, we undertook laboratory and numerical investigations of failure of a simulated boulder-rich granular surface as regional slopes increase slowly in a quasi-static manner. A slow increase in slope is expected as Bennu rotationally accelerates due to the YORP effect (Hergenrother et al., 2019; Nolan et al., 2019). The laboratory investigations allowed for a broad range of particle sizes in the granular bed, but were limited to Earth-gravity acceleration (1 *g*). On the other hand, the numerical studies, which use a soft-sphere discrete element method within the highly efficient parallel tree code pkdgrav (D. Richardson, 2000; Schwartz et al., 2012; Stadel, 2001; Zhang et al., 2017, 2018), can explore conditions under Bennu's microgravity but are limited in the number of particles that can be simulated with reasonable computational times. The simulation, therefore, considers the case where individual particles are large relative to the thickness of the granular bed, and provide a reference point for how well the continuum-based *FS* model might work when the granular bed structure deviates from a continuum. So, the experimental and numerical investigations are complementary and together can allow us to better understand Bennu's surface dynamics and current evolution.

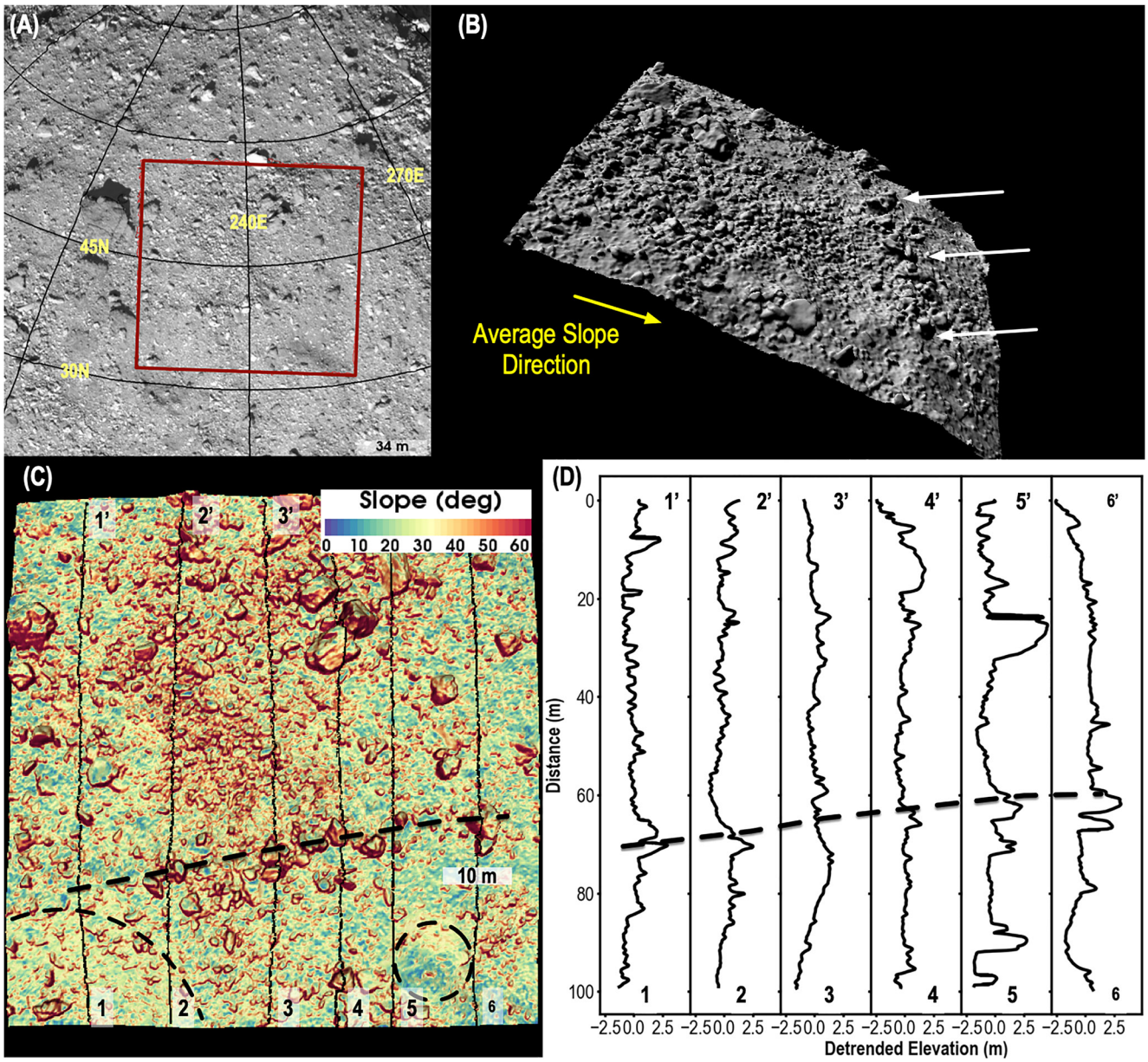

Figure 6. (a) Detailed global and (b and c) regional view of region T2 identified in Figure 1. An OSIRIS-REx Camera Suite image obtained on 4 April 2019 at 20:36:20 UTC (a) shows the location of local digital terrain model used to study the terrace in (b and c). The arrows and dashed line highlight the terrace, which is evident in detrended elevation profiles where a linear function is fit to and subtracted from the elevation as a function of distance (d). Candidate craters are visible as dashed circles in (c).

4.1. Laboratory Investigation

The laboratory investigation made use of a cohesionless gravel with a bimodal particle distribution that is intended to mimic the properties of the surface material seen on Bennu. The particles used were measured using a Retsch Technology Camsizer, which is an imaging-based particle size analyzer, where the smallest of all maximum observed lengths observed across a particle was attributed to the particle size, while the longest length was used to determine the average sphericity (defined as 4π times the area of each particle's projection divided by the square of the measured circumference of the particle projection). The analysis showed that our gravel has a peak diameter of 1.3 mm for 18% of its incremental volume, and 4.4 mm for 32% of its incremental volume. The full range of particle sizes spans from 0.07 to 8 mm. The overall gravel has a mean particle aspect ratio of 0.68, with the smaller particles being slightly more rounded (sphericity near 0.83) relative to the larger ones (sphericity near

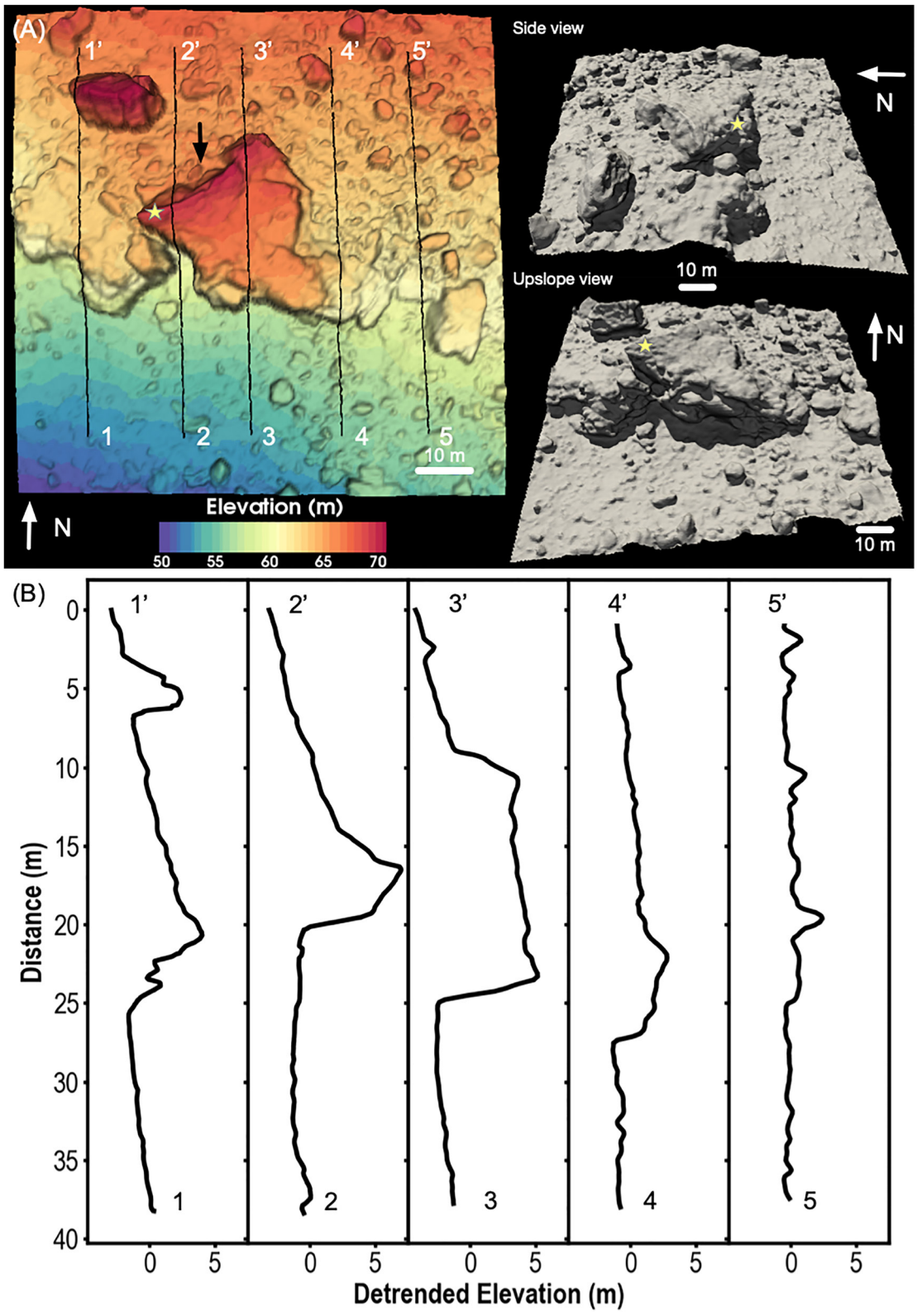

Figure 7. Detailed OLA-derived DTM (a) of a boulder constituting a terrace located at 85.9°E and 68.5°N. The large 25-m-diameter boulder in the middle of the DTM makes up part, but not all, of the terrace step seen in the DTM and in the profiles (b), where a linear function is fit to and subtracted from the elevation as a function of distance, and the residual (detrended elevation) is shown. The side and upslope views in (a) show evidence for upslope debris retention that embays the boulder (black arrow) and downslope undercutting of the boulders. The yellow stars in (a) mark the same location in each view.

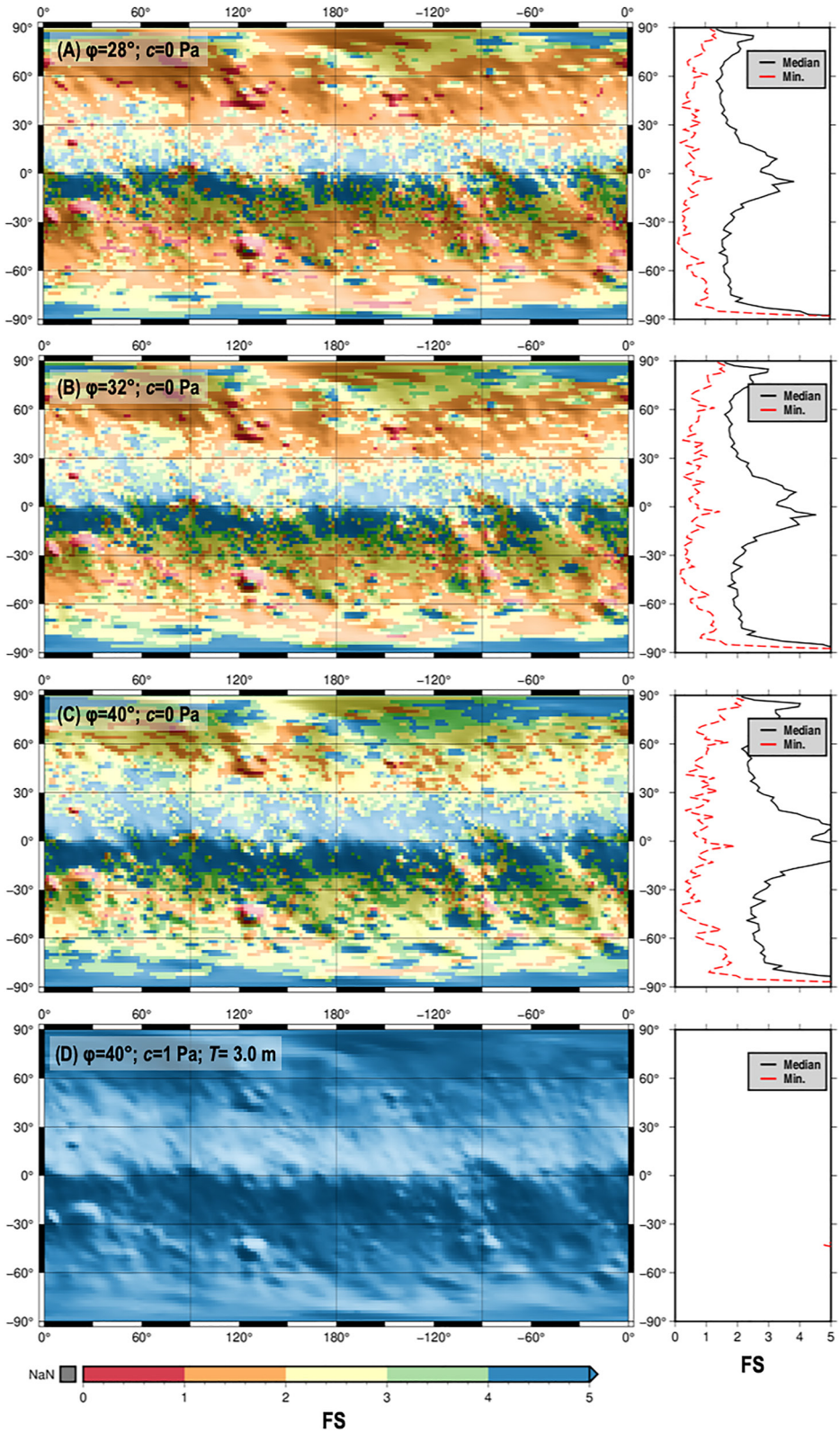

Figure 8. Factor-of-safety assessment of Bennu's surface stability plotted on a global map (left) and by latitude (right) shows that for most cohesionless cases (a–c), the surface is very likely failing currently ($FS < 1$), especially poleward of ±30° degrees of latitude in both hemispheres. The presence of even small amounts of surface cohesion (d), however, completely suppress such failure. The *FS* results that were computed with the low resolution 12 m GDTM (see text) was re-sampled using 2° by 2° bins.

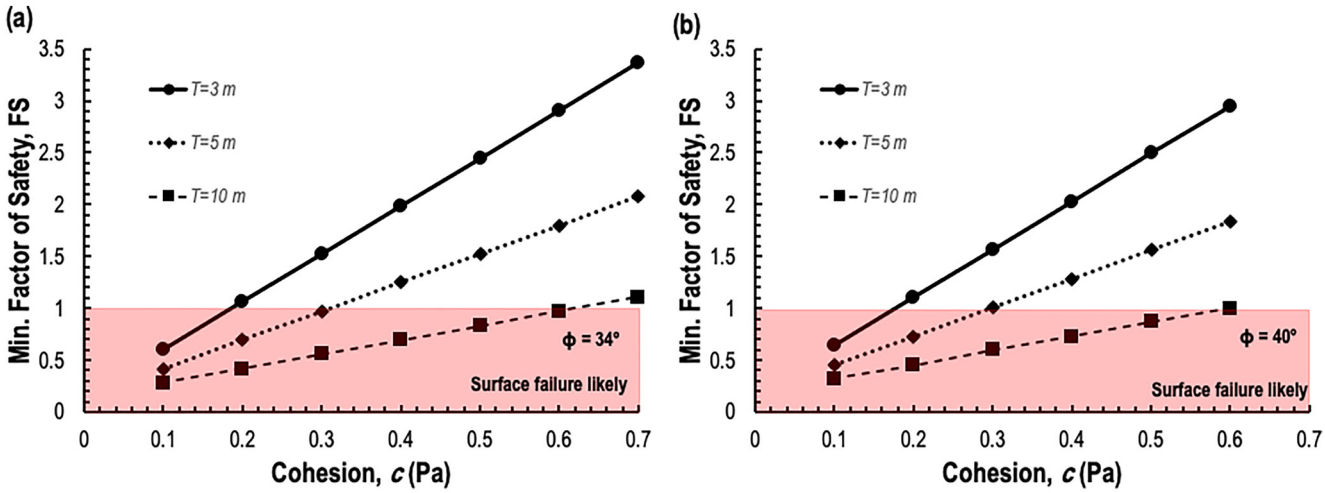

Figure 9. Minimum *FS* value across the surface of Bennu as a function of cohesion, *c*, for different unconsolidated regolith layer thicknesses, *T*, and ϕ equal to (a) 34° and (b) 40°.

0.8). Such increase in roundness with decreasing particle size is common and expected even for many natural granular materials on Earth (e.g., Das & Sivakugan, 2016), and is plausible for impact-evolved asteroid regolith (e.g., Cintala & Horz, 1988). Our gravel mean aspect ratio is consistent with the mean range of 0.63–0.72 observed for boulders on Itokawa, Ryugu, and Eros (Michikami & Hagermann, 2021, and references therein), and the value of 0.7 observed for sampled Itokawa regolith (Tsuchiyama et al., 2011). The angular nature of the gravel is reflected in the measured angle of repose of the gravel, which is steep at 38 ± 3°. The bulk density of this material is 1,652 ± 2 kg/m^3; individual grains measure 2,394 ± 2 kg/m^3.

The coarse component of our gravel is intended to illustrate the behavior of the majority of the surface rocks and boulders seen on Bennu, while the finer fraction is intended to represent the finer particles that can be observed below the layer of coarse particles (Molaro et al., 2020), especially around and inside some of the small craters (R. T. Daly et al., 2020; DellaGiustina et al., 2020; Rizos et al., 2021). We also placed one relatively large rock on the surface for five of the experiments to understand how large boulders, which are pervasive on Bennu and influence the regional geology (M. G. Daly et al., 2020; Jawin et al., 2020), could impact the evolution of our experimental surfaces. Although the bulk density of the experimental gravel (and of the numerical particles in Section 4.2) does not match the global bulk density of 1,194 ± 3 kg m^{-3} reported for Bennu, the gravel's porosity of 31% ± 2% is within the 25%–50% range possible for Bennu (Barnouin et al., 2019; M. G. Daly et al., 2020). The surface features (e.g., scarp, surface flow, pile-up) that might result from slope failure in dry, low-cohesion ($c \approx 0$ Pa) granular media probably do not depend significantly on porosity differences, except maybe to influence the periodicity of pile-up or surface compression features. As important, if not more so, is the friction angle of the gravel, whose magnitude is consistent with expectations based on the sub-angular to angular nature of the surface rocks and boulders on Bennu's surface (see Section 3 and DellaGiustina et al., 2020).

We undertook nine near-identical experiments. The experiments consisted of placing a 0.05–0.1 m layer of gravel within slightly inclined box that measured 0.91 m by 0.41 m by 0.265 m, which was then inclined further to a shallow angle of about 25°. We then flattened the slope of the gravel to match the box slope. We partially buried the relatively large rock (0.1–0.15 m diameter) in the gravel, to a depth of ~0.02 m. The gravel surface was flattened to align with the inclined slope. The box slope was then slowly increased using a hand crank to well over 50°. The changes in the gravel surface were noted using a video camera, and for one experiment, topography changes were assessed using a hand-held Artec Eva 3D scanner. The scanner is accurate to 0.0005 m.

Figure 10 provides a qualitative view of the surface changes observed in the experiments as the slope was increased. Initially, discrete particles tumbled and eventually stopped after a few rolls. In some instances, particles rolled up onto the large rock. With additional increases in surface slope, local slumps occurred, often initiated where by luck the finer-fraction of the gravel had accumulated just below the surface. This occurs around when $FS \leq 1$ (slopes $\geq 38 \pm 3°$). The resulting morphologies ranged from small V-shaped scarps (Figure 11)

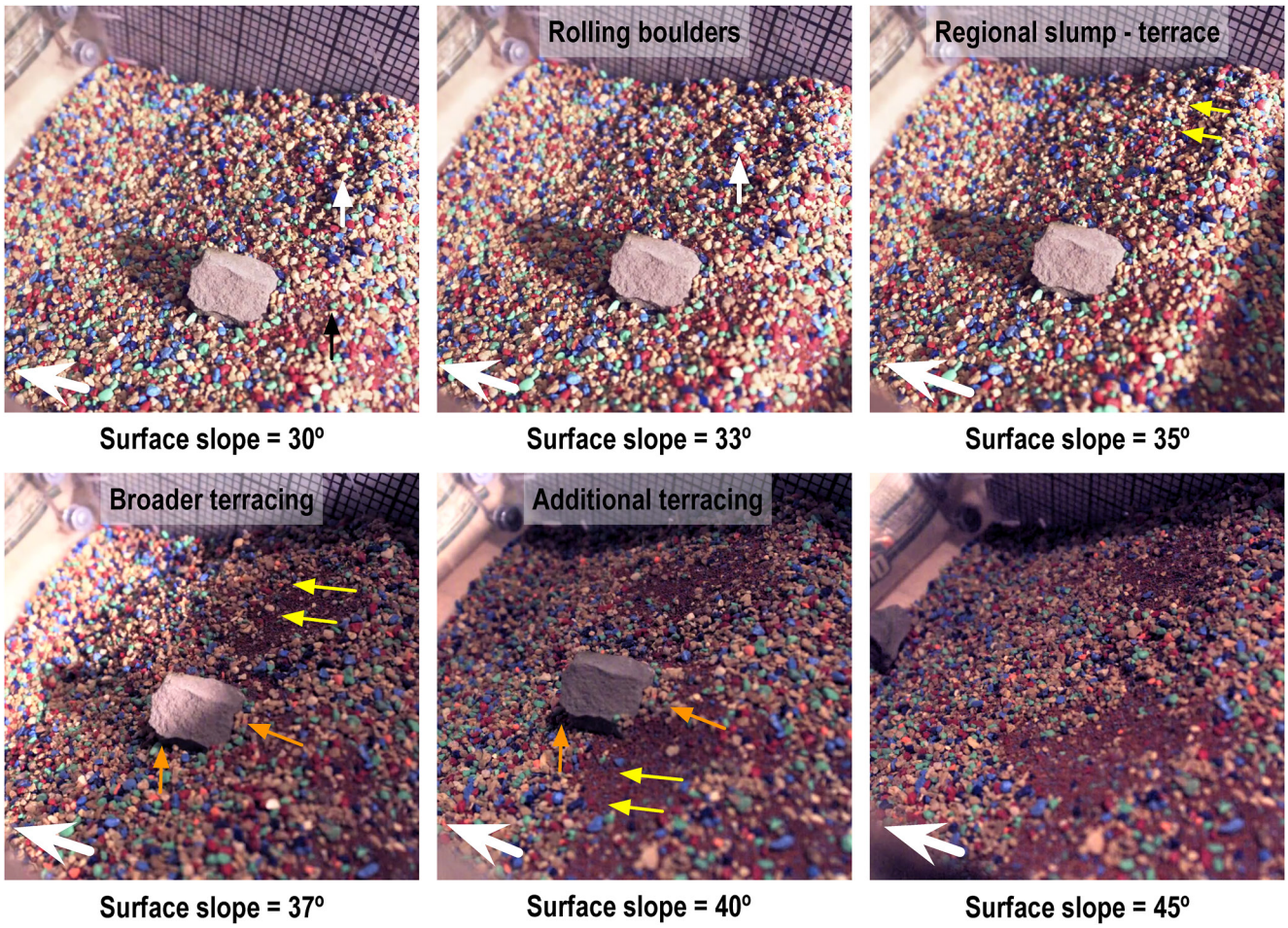

Figure 10. Laboratory results showing changes in a granular surface with slowly increasing slope. We observe initial toppling of gravel between frames (thin white arrow), followed by localized and then broader regional scarp formation (yellow arrows). We also see evidence for accumulations above and undercutting below the larger rock (orange arrows). The large white arrow indicates the downslope direction. The major and minor lines in the top grid are separated by 0.05 and 0.01 m, respectively; particles sizes used are described in Section 4.1.

to a broader scarp 1/4 to 1/3 of the box width. The slumps exposed finer and smoother material underneath and accumulated coarser gravel at their downslope ends, consistent with expectations (e.g., Iverson, 1997). Subtle terrace-like structures are apparent at both the top and bottom of the scarps. We observed build-up of material on the upper slopes of the larger rocks, and undercutting and removal of material on their downslope sides. Two out of five times, the larger rock tumbled when the slope was well in excess of the 40°. In one experiment, the slope decreased quickly due to a prior slump and the rock stopped (Figure 11); otherwise it continued down to the low-elevation end of the apparatus. When the rock collided with the end of the apparatus, the box edge knocked the rock around so that its long-axis end-up parallel to the edge of the apparatus.

The topographic data (Figure 11) collected by the 3D scanner during one of the experiments indicate how localized scarp formation produces one type of terrace in the profiles of the surface as the slope is slowly increased. When surface failure begins, the terraces derived from scarps include an upslope ridge followed by a depression that ends in another upslope ridge. The steepest portions of the terraces, usually just below the upslope ridge, are smoother relative to the surrounding terrain. As the surface slope continues to increase, material loss or undercutting is visible below the larger rock, while there is an increase of material upslope (see box slope of 45° in Figure 11c). With additional surface failure, the terraces span a larger horizontal portion of the experimental box. Additional scarp-derived terraces that form further downslope are less pronounced and more rough in nature. Another type of terrace (Figures 11d and 11f), which is also less well pronounced, can form due to gravel pile-ups that compresses on themselves to form surface undulations or terraces, as the local slope across

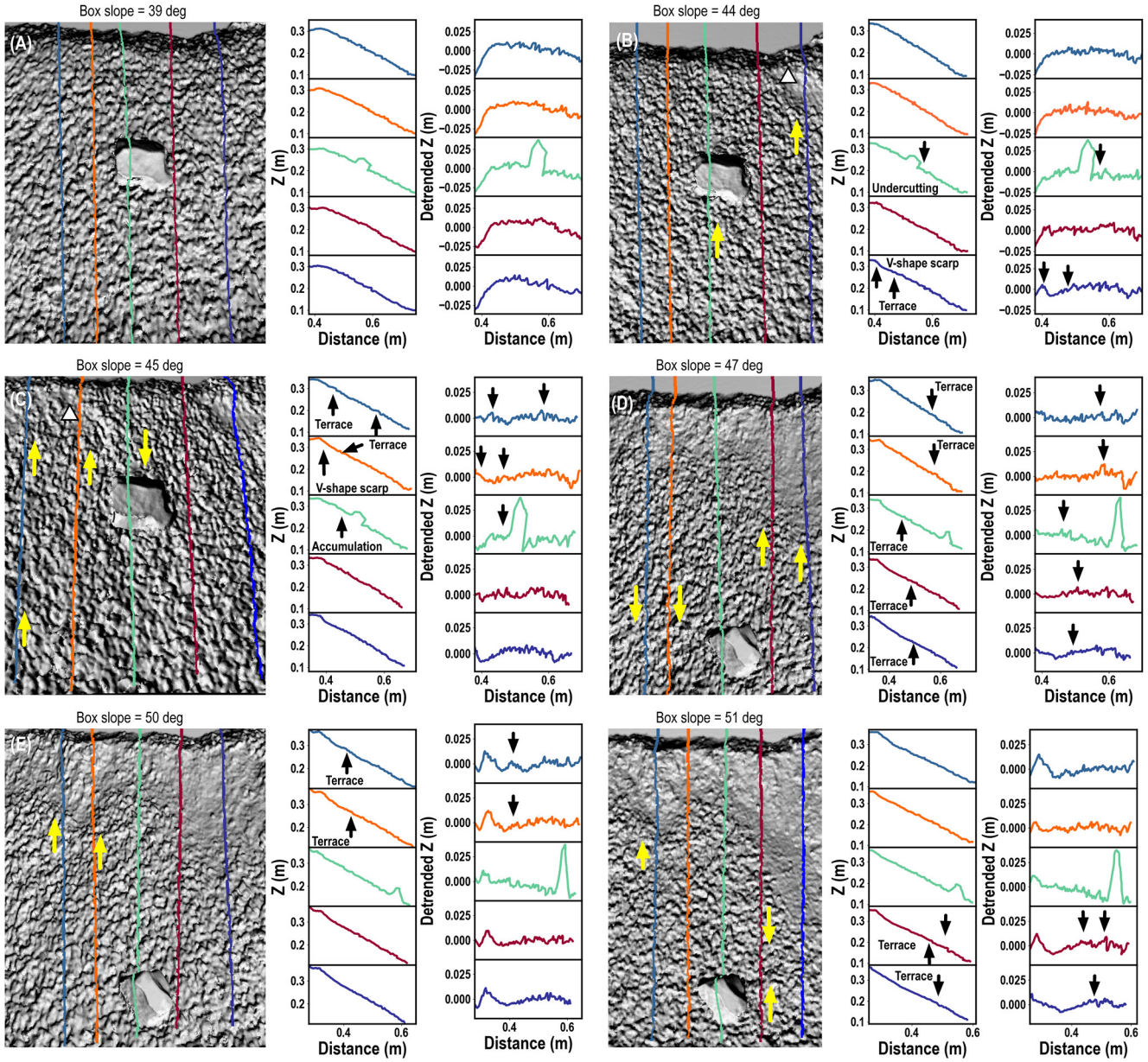

Figure 11. Changes in surface topography of experiments with increasing slope, showing scarps that create terraces, and evidence for downslope undercutting around the large rock. In each panel, colored lines overlaid on the view from above (left) correspond to profiles of the same color (middle) and their detrended versions (right). For the detrended profiles, a linear fit to the middle profile is removed to show residual heights. Yellow and black arrows show new terrace formation and undercutting. White triangles show the location of downslope-opening V-shaped scarps.

the apparatus shallows due to prior failure-driven surface re-adjustments. The large rock that tumbled downslope in this particular experiment, was the one that stopped before it reached the edge of the experiment, and rotated, with its long axis pointing more or less along the direction of slope.

The experiments show surface characteristics that are consistent with observations of Bennu. In all the laboratory experiments, individual gravel initially toppled over as the slope slowly became unstable. This results in a creeping downslope motion of the surface. Evidence for toppling and some downslope motion of smaller (≤1 m diameter) boulders has been reported for Bennu (M. G. Daly et al., 2020; Jawin et al., 2020; Walsh et al., 2019), including long axes preferentially pointing in the slope direction (Schwartz et al., 2019). On Ryugu, evidence for boulder toppling has also been reported, but the orientation differs from that seen on Bennu, where the long axes of boulders tend to lie perpendicular to the slope direction (Ebihara et al., 2021). Terrestrial studies (Abrahams

et al., 1990; Bertran et al., 1997) indicate that boulders rolling down a surface will have their long axis perpendicular to the slope direction, but when coming to a final stop will frequently slide and turn such that their long axes are re-orientated parallel to the slope direction. This process of reorientation occurred for the large rock in at least one of our experiments.

The experiments also indicate how regional scarps can generate the terrace structures visible on Bennu. When first formed in the experiments, at angles where $FS \sim 1$ (slopes ~38.5°), these scarps tend to be somewhat confined regionally across the slope, sometimes generating a V-feature that opens downslope. As the slope increases, the scarps span a greater width of the experimental gravel bed, and look much more like a terrace, but can undulate somewhat across the slope. At even greater slope, more than one set of terraces can form across the slope, sometimes as a pile-up terraces. These observations are very similar to what we see with the Bennu terraces, including somewhat longitudinally extensive features, the presence of more than one set of terraces as one moves downslope, and some evidence for very localized V-shaped slope failure along a terrace. Also, on Bennu, some of the steepest portions of the terraces appear lacking in coarse particles, while rock and boulder pile-ups form near other terrace crests, consistent with the experimental results. Some pile-up terraces, consisting of boulder aggregations that compress on themselves to form surface undulations, may also exist on Bennu (e.g., at top of regions shown in Figure 6).

The influence of the largest objects is evident both on Bennu (boulders ≥30 m; M. G. Daly et al., 2020; Jawin et al., 2020) and in the experimental gravel beds (large rock). In both cases, these retain material upslope, whereas they are undercut as material is removed from their downslope side.

4.2. Numerical Investigation

4.2.1. Simulation Setup

Simulations were performed using a similar setup as the experiments described in Section 4.1. We used a non-vertical gravity vector, accounting for its evolution as a function of time to reproduce the increasing slope from spin-up. The magnitude of the gravity vector was chosen to be similar to that on Bennu, that is, $10^{-5}g$ where g is the magnitude of the gravity on Earth. In our simulation scenario, a box with dimensions of $80 \times 60 \times 15$ m was used to carry the granular bed, where the largest dimension is the downhill one and the smallest dimension is the depth of the box. We considered meter-sized particles and assumed a Gaussian size distribution with a mean radius of 0.5 m, a standard deviation (σ) of 30%, and a cut-off at 1σ. These particles, thus, mimic the behavior of a granular bed composed mostly of larger boulders on Bennu. The simulated particles have gravel-like properties represented by frictional coefficients set to correspond to an angle of repose of 38.5° (Thuillet et al., 2018) and no cohesion ($c = 0$ Pa).

To generate the granular bed, we simulated the free fall of the particles under a vertical gravity field with a magnitude of $10^{-2}g$ to accelerate the process, then we continued the computation until the bed relaxed. After relaxation, we switched the magnitude of gravity to a Bennu-like value of $10^{-5}g$. Once again, we continued the computation to let the bed relax, and then we flattened the top surface by removing those particles whose centers sat above ~10 m from the bottom of the box. This 10 m bed thickness was chosen to equal the maximum depth of unconsolidated surface materials measured near Bennu boulders (Jawin et al., 2020). All the particles at the base of the box are stuck to it, but maintain otherwise the same frictional properties as the rest of the particles within the box. We inclined the gravity vector to 30° from the surface normal, which is well under the critical angle of repose of our gravel-like material. The relaxed bed, with an inclination of 30°, is shown in the top frame of Figure 12. The particle density is 2,430 kg/m^3, and the bulk density of the granular bed is 1,650 kg/m^3 (close to the one used in the laboratory experiments).

4.2.2. Simulation Results

In the first simulation, we gradually increased the inclination angle from 30° up to 60°. Figure 12 presents the evolution of the granular bed during this process. The inclination was increased slowly stepwise by 0.5° every 100,000 iterations, that is, about every 630 s, or 10.5 min. After about 5 hr and an inclination angle of 44.5°, we observed that some particles in several local surface regions began to tumble downhill. The discrete size of the particles (~1/10 of the granular bed) and the micro-g likely contribute to increasing the stability of the slope relative to the FS expectation near 38.5°, further substantiating that cohesion is unlikely to be very important on

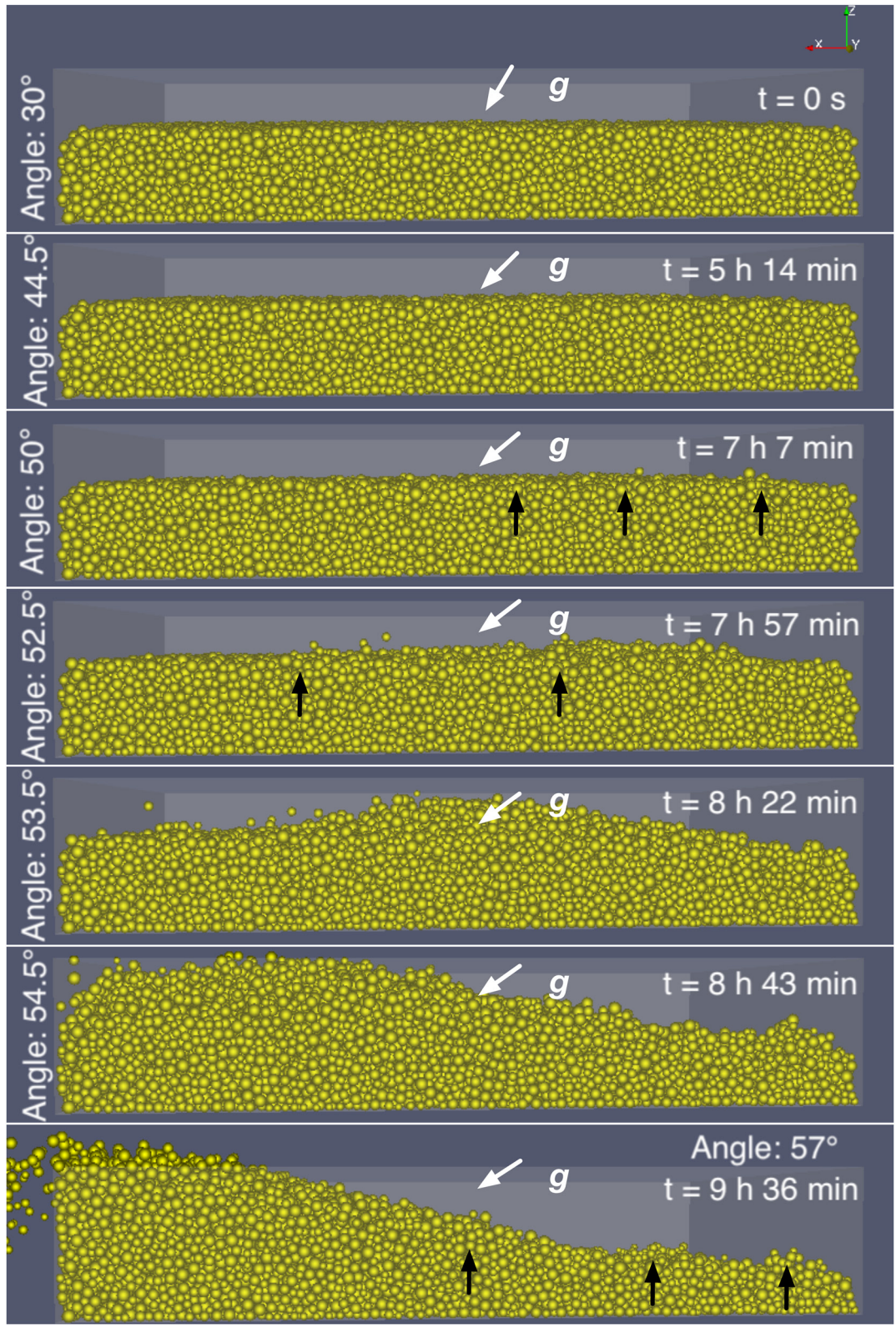

Figure 12. Snapshots of a simulation during which the gravity vector is inclined step-wise by an additional 0.5° every 10.5 min. At $t = 0$ s, the particle bed is 10 m thick. Each particle is 0.5 m in radius, and the box is 80 m long. The inclination angle and the time relative to the beginning of the simulation at 30° are indicated in each frame. Black arrows indicate the formation of temporarily stable surface undulations that represent terraces.

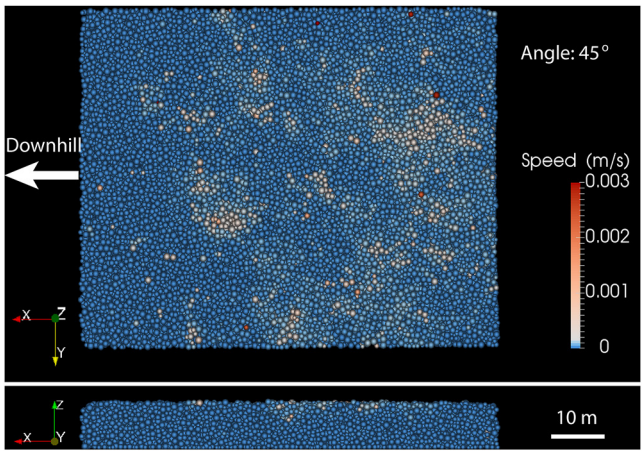

Figure 13. Speed distribution of the surface layer (top and side views) of the granular bed at the moment when the inclination angle is increased to the termination angle (45° in this case).

Bennu. With a larger inclination, near 50°, small undulations formed that represent subtle terraces. As the inclination increased to ≈52.5°, massive landslides were initiated and the whole granular bed collapsed, leading to the formation of more pronounced regional terrace crests near the top of the slope (Figure 12 bottom).

To analyze the mobility of the granular bed at different inclination angles, we considered different termination angles between 43° and 53°. The simulations were started at identical slopes and stopped after the given termination angle value was reached. The granular bed then evolved under the termination inclination. Prominent movements of particles on the surface were identified for all these cases.

Figure 13 shows the speed distribution of the particles on the surface at the moment when the bed is inclined to a termination angle of 45°. It is evident that the surface failure is highly heterogeneous due to the nonuniform interactions at particle scales. This regional surface failure results in the formation of some localized scarps and eventually leads to terraces (such as those shown in Figure 12).

It is also notable from Figure 13 that the particles in the subsurface layer near the base of the bed (in the Z direction) are unaffected by the inclination changes. We computed the average displacements in 0.5-m-thick increments (layers) of the granular bed cross-section (parallel to the initial surface plane of the granular bed) between the initial and the final states for different termination angles (Figure 14). As seen in the terrestrial case (e.g., GDR MiDi, 2004), the higher the inclination angle, the larger the displacements of the top layers, and the deeper the locations of the mobilized particles. The upper particles moved much faster on the bed than the lower ones. For the termination angles of 43°–50°, the displacements of the particles increase monotonically with height, whereas for a larger termination angle, the displacements of the top 4 m is practically identical, which is indicative of bed collapse. For smaller termination angles between 43° and 45°, the profiles of the displacement and final distribution of particles are very similar, indicating that, after some regional failure, the bed relaxes to a new stable state. Particles at depths below 8 m barely move in all the cases, suggesting that surface failure should be able to cause maximum height changes of 5–8 m in Bennu-like gravity conditions. This magnitude is on the order of the changes in height associated with terraces on Bennu (1–5 m), and similar to the average 5 m-thick deposits reported near some Bennu boulders (Jawin et al., 2020).

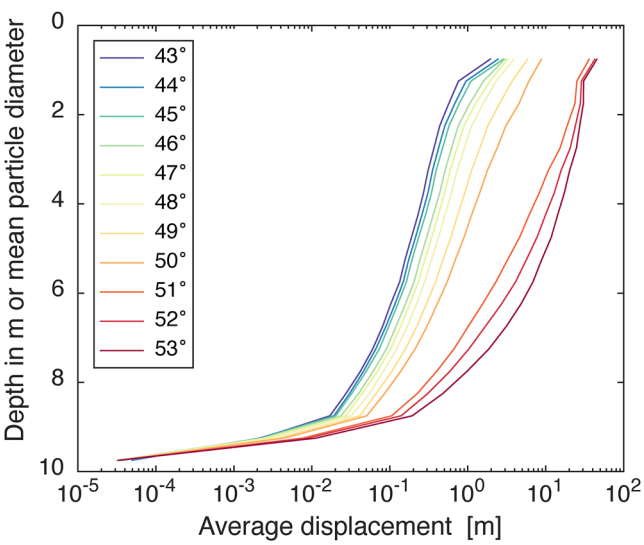

Figure 14. Average displacements in the simulated granular bed as a function of depth below the initial top edge of the box, for different termination angles. Averages were taken over 0.5 m thick layers; averages taken over other layer thicknesses did not change the observed profile shapes.

Although the gravity and particle size conditions varied between the numerical simulations and the laboratory results, we observed consistent behavior in both settings, such as individual particles toppling and regional failures. The regional failures produced subtle undulations in the bed at small inclinations, and wider terraces with increasing slope. Eventually, as the slope steepens further, the failure is catastrophic. Most of the material is deposited at the bottom of the slope, while some new terraces begin to form upslope. We anticipate that the numerical simulations would lead to additional terrace formation if it were numerically feasible to consider a broader, less uniform size range of particles leading to more common pile-up terraces formed behind individual large particles. The numerical results do show that, even if the surface is cohesionless, only the top 5–8 m of the unconsolidated surface is expected to fail and flow downslope.

5. Terrace Formation on Bennu: Synthesis and Conclusions

Elevation and slope measurements of Bennu's surface show evidence for extended terraces that are present at mid- to high latitudes above ±20°. These show up as step-like sets of flattish benches in the topography followed by

steep drops in slope as one moves down in elevation and latitude from the pole toward the equator. The topography associated with these terraces is fairly subtle (1–5 m) but not insignificant (equivalent in terms of dynamic range to 0.3–1.5 km features on Earth). The terraces often possess evidence for accumulations of boulders of all sizes on their crests, and can, in some instances, be smooth beyond the ridge on their steepest portions.

A geotechnical stability analysis indicates that the regions on Bennu where the terraces are observed are likely unstable under Bennu's current accelerating spin state. The continued increases in the spin rate will likely lead to continuing surface failures. The region where the surface is unstable is limited to the mid- to high latitudes, but will move to lower latitudes with increasing spin. The stability analysis also shows that surface flow and terrace formation would not occur if the surface has even minimal cohesion (as small as 0.2 Pa for a 3 m thick flow). Such a lack of surface motions is inconsistent with the plausible surface failure origin of Bennu's terraces and other clear evidence for mass movement on Bennu. Therefore, Bennu's top 10 m of surface material is probably cohesionless.

Consistent with this assessment, Bennu's terraces strongly resemble the scarps generated on cohesionless granular beds in laboratory and numerical investigations as their slopes increase very slowly. Both the 1-*g* laboratory experiments and the Bennu-like *g* numerical models show that creeping failure via particle tumbling and localized scarping dominate the surface changes until very high slopes are reached and catastrophic mass movements occur—similarities that confirm in the case when there is no cohesion that reducing gravity does not meaningfully alter the process of failure. The terraces produced in the numerical calculations have less height than their counterparts in the experiments, possibly as a consequence of the lower *g*, which could explain why Bennu's terraces are subtle. Also, numerical simulations show that the thickness of unconsolidated material that can flow on Bennu in its low gravity environment is limited to 8 m, which may impose limitations on terrace formation. Considering the stability analysis together with the numerical and laboratory data indicates that terraces are probably forming currently; the surface of Bennu is slowly failing by creep as Bennu's spin rate (and thus surface slope) increases.

The lack of cohesion at Bennu's surface and near-surface is not inconsistent with the previous finding that Bennu needed 1 Pa of cohesion for the formation of its equatorial bulge (Scheeres et al., 2019). Surface debris on Bennu is expected to have fewer fine particles that drive surface cohesion than at depth, owing to meteoroid impact gardening, thermal fragmentation (e.g., Molaro et al., 2020), and electrostatic lofting (Hartzell, 2019; Schwan et al., 2017), all of which can lift fines off the surface, and solar radiation pressure, which blows the fines into space. Such processes work together to release fine particles from the surface that do not return. Also, models of asteroid spin-up (Zhang et al., 2018) show that even in asteroids with small interior cohesion such as Bennu, their surface material packs less effectively, leading to an essentially cohesionless surface that can more readily flow.

Taking all evidence together, we contend that Bennu's current surface evolution is the result of surface creep that forms terraces. As the asteroid spins up, some of the boulders and rocks topple downslope and slide, often re-orientating. This process exposes new boulders and rocks that re-supply the creep process as slopes continue to increase. In some instances, localized failure occurs to produce V-shaped scarps. As Bennu's slopes steepen due to spin-up, these scarps extend in size to become terraces that span roughly along lines of latitude. Failures occur perpendicular to the slope along different lines of latitude, giving a step-shape to the asteroid's surface. In regions where the surface material is more homogeneous in size (below −30° latitude), the terraces become more uniform in height and spacing. In some areas, rocks can pile up behind a large boulder to produce a regional terrace that exceeds the lateral span of the boulder. The rocks that pile up onto such a feature can create additional surface undulations or terraces behind it. These latter type of pile-up terraces are more subtle and rocky in nature than other terraces observed.

The ongoing creep on Bennu implies that surface debris is continuously being removed from mid-to-high latitudes and deposited at lower elevations, as posited by Jawin et al. (2020). Not all of the debris that could be mobilized from higher latitudes during the current epoch of YORP spin-up has yet made its way to the lowest elevation, as evinced by the fact that massive landsliding of Bennu at the mid- to high latitudes has not yet occurred. This probably helps explain why, at the mid- to high latitudes where terraces are found, fewer large craters (≥30 m in diameter) are apparent than at low latitudes below 30° (Walsh et al., 2019). The creep processes is removing over-steepened crater rims upslope, and filling crater interiors downslope, thereby removing them. The cumulative effects of creep on putatively younger, intermediate-sized (10–30 m in diameter) craters appears

to be small (Bierhaus et al., 2022; Jawin et al., 2022). This may be because creep is a slow but long-lived. Its cumulative effect is probably limited to the top meter of the surface and just barely affects the rate of formation of these 10–30 m in diameter-sized craters. Creep, therefore, is probably too slow to keep up with the pace of formation of craters below 2 m because the observed deficit in this size range appears to occur at all latitudes more or less equally (Bierhaus et al., 2022). Only further study, where crater degradation is considered through other means (e.g., space weathering; DellaGiustina et al., 2020; Jawin et al., 2020; Rizos et al., 2021) will the importance of surface creep in modifying crater <2 m be fully determined.

Creep exposes fresh rock surfaces, which are likely to be more hydrated (Hamilton et al., 2019) than surfaces exposed for longer durations. This may explain the greater variation in surface color and albedo observed across Bennu (DellaGiustina et al., 2021) relative to other asteroids such as Ryugu, which does not have observable terraces like those on Bennu (e.g., Kitazato et al., 2019; Sugita et al., 2019).

Does surface creep play any role in the particle ejection events observed at Bennu by OSIRIS-REx (Lauretta, Hergenrother, et al., 2019)? Three main mechanisms have been proposed as the most plausible to explain the observed particle ejection phenomenon (Lauretta, Hergenrother, et al., 2019): sudden volatile release of adsorbed water in phyllosilicates from newly exposed material, thermal fatigue and fracturing of surface rocks (Delbo et al., 2014; Dombard et al., 2010; Molaro et al., 2020), and impacts by meteoroids (Bottke et al., 2020). The lattermost is unlikely to be influenced by surface creep in any way, but particle ejection by volatile release and thermal fragmentation could be.

A slight preference is observed for particle ejection from low latitudes (Hergenrother et al., 2020; Lauretta, Hergenrother, et al., 2019, and references therein). These low latitudes usually possess small slopes (Figure 2), and refreshing by surface creep is less likely. The observed preference may, therefore, favor thermal fragmentation, which is more efficient if a rock is exposed to thermal cycles for a longer time (Delbo et al., 2014; Dombard et al., 2010; Molaro et al., 2020). At mid-latitudes, where surfaces are more frequently refreshed by creep, volatile release-related ejection could be important, and fracturing of rocks via thermal fatigue and fracturing may be hindered. The slight preference observed for particles ejection from low latitudes (Hergenrother et al., 2020; Lauretta, Hergenrother, et al., 2019, and references therein) thus favors thermal fatigue processes for particle ejection and counters particle release mechanisms that depend upon adsorbed water.

Can any additional inferences be made regarding the importance of surface creep for particle ejection on Bennu via comparisons to spacecraft observations obtained at other small near-Earth asteroids, such as Ryugu and Itokawa? Both of these celestial objects should experience similar thermal fatigue and meteoroid bombardment processes. Nevertheless, the answer is not really. Particle ejection similar to that seen on Bennu has not been reported at Ryugu or Itokawa, but the null detection does not preclude its existence: it could be explained by lower-resolution imaging capabilities aboard the Hayabusa and Hayabusa2 spacecraft that visited these other asteroids (Hergenrother et al., 2020) and non-ideal observing conditions such as low phase angle and lack of an orbiting attitude. Conversely, these less favorable observation capabilities and conditions do not mean that we can assume particle ejection activity is present, but simply undetected, on Ryugu and Itokawa. Both Hayabusa and Hayabusa2 included a wide-angle imager (with FOV of >60°) that may have provided some opportunity to see particles far from the asteroid. Itokawa and Ryugu are not currently undergoing the extensive creep-driven surface failure that Bennu is experiencing because of their slow rotation rates. But these slow rotation rates might actually enhance the size of the particles ejected and thereby facilitate their detection if they are the result of thermal fatigue: A thermal wave can penetrate deeper during the longer day-night cycle associated with slower spin. The null detections at Ryugu and Itokawa may indicate, therefore, that the material properties (e.g., rock strength, porosity, volatile presence) of Bennu's surface are different, that Bennu's resurfacing plays an important role in enhancing the production of ejected particles, that Bennu's greater spin rate (leading to lower surface gravity) facilitates particle ejection and detection, or that we still have work to do to understand the mechanisms of particle ejection. We can only conclude that further exploration of small bodies is warranted to establish a connections between surface activity evinced by particle ejections and ongoing surface changes due to creep.

Data Availability Statement

OLA (M. Daly et al., 2019) and OCAMS (Rizk et al., 2019) data are available via the Planetary Data System. The OLA v20 shape model is published in M. G. Daly et al. (2020) and available via the Small Body Mapping Tool (SBMT) at http://sbmt.jhuapl.edu/. The SBMT was used to generate many of the presented figures.

Acknowledgments
This effort was supported by NASA under Contract NNM10AA11C issued through the New Frontiers Program and by the Canadian Space Agency. Y. Zhang acknowledges funding from the Université Côte d'Azur "Individual grants for young researchers" program of IDEX JEDI. P. Michel., Y. Zhang, F. Thuillet acknowledge support from the French space agency CNES, from the European Union's Horizon 2020 research and innovation program under grant agreement No 870377 (project NEO-MAPP), and from Academies of Excellence: Complex systems and Space, environment, risk, and resilience, part of the IDEX JEDI of the Université Côte d'Azur. The authors would like to thank Tatsuhiro Michikami and one other anonymous reviewer for their comments, which greatly improved this manuscript.

References

Abrahams, A. D., Soltyka, N., Parsons, A. J., & Hirsch, P. J. (1990). Fabric analysis of a desert debris slope: Bell Mountain, California. *The Journal of Geology*, *98*(2), 264–272. https://doi.org/10.1086/629397

Barnouin, O. S., Daly, M. G., Palmer, E. E., Gaskell, R. W., Weirich, J. R., Johnson, C. L., et al. (2019). Shape of (101955) Bennu indicative of a rubble pile with internal stiffness. *Nature Geoscience*, *12*(4), 247–252. https://doi.org/10.1038/s41561-019-0330-x

Barnouin, O. S., Daly, M. G., Palmer, E. E., Johnson, C. L., Gaskell, R. W., Al Asad, M., et al. (2020). Digital terrain mapping by the OSIRIS-REx mission. *Planetary and Space Science*, *180*, 104764. https://doi.org/10.1016/j.pss.2019.104764

Barnouin-Jha, O. S., Cheng, A. F., Mukai, T., Abe, S., Hirata, N., Nakamura, R., et al. (2008). Small-scale topography of 25143 Itokawa from the Hayabusa laser altimeter. *Icarus*, *198*(1), 108–124. https://doi.org/10.1016/j.icarus.2008.05.026

Bertran, P., Hétu, B., Texier, J.-P., & Steijn, H. V. (1997). Fabric characteristics of subaerial slope deposits. *Sedimentology*, *44*(1), 1–16. https://doi.org/10.1111/j.1365-3091.1997.tb00421.x

Bierhaus, E. B., Trang, D., Daly, R. T., Bennett, C. A., Barnouin, O. S., Walsh, K. J., et al. (2022). Crater size-frequency distribution on Bennu reveals impact armoring and young surface. *Nature Geoscience*. https://doi.org/10.1038/s41561-022-00914-5

Bottke, W. F., Moorhead, A. V., Connolly, H. C., Hergenrother, C. W., Molaro, J. L., Michel, P., et al. (2020). Meteoroid impacts as a source of Bennu's particle ejection events. *Journal Of Geophysical Research: Planets*, *125*(8), e2019JE006282. https://doi.org/10.1029/2019JE006282

Cheng, A. F., Barnouin, O. S., Prockter, L., Zuber, M. T., Neumann, G., Smith, D. E., et al. (2002). Small-scale topography of 433 Eros from laser altimetry and imaging. *Icarus*, *155*(1), 51–74. https://doi.org/10.1006/icar.2001.6750

Cintala, M. J., & Horz, F. (1988). The effects of impact velocity on the evolution of experimental regoliths. *Lunar and Planetary Science Conference Proceedings*, *18*, 409–422.

Daly, M., Barnouin, O., Espiritu, R., & Lauretta, D. (2019). *Origins, Spectral Interpretation, Resource Identification, Security, Regolith Explorer (OSIRIS-REx): OSIRIS-REx Laser Altimeter Bundle*. NASA Planetary Data System. Retrieved from https://arcnav.psi.edu/urn:nasa:pds:orex.ola

Daly, M. G., Barnouin, O. S., Dickinson, C., Seabrook, J., Johnson, C. L., Cunningham, G., et al. (2017). The OSIRIS-REx laser altimeter (OLA) investigation and instrument. *Space Science Reviews*, *212*(1–2), 899–924. https://doi.org/10.1007/s11214-017-0375-3

Daly, M. G., Barnouin, O. S., Seabrook, J. A., Roberts, J. H., Dickinson, C., Walsh, K. J., et al. (2020). Hemispherical differences in the shape and topography of asteroid (101955) Bennu. *Science Advances*, *6*(41). https://doi.org/10.1126/sciadv.abd3649

Daly, R. T., Bierhaus, E. B., Barnouin, O. S., Daly, M. G., Seabrook, S. A., Roberts, J. H., et al. (2020). The morphometry of impact craters on Bennu. *Geophysical Research Letters*, *47*(24). https://doi.org/10.1029/2020GL089672

Das, B. M., & Sivakugan, N. (2016). *Fundamentals of geotechnical engineering*. Cengage Learning.

Delbo, M., Libourel, G., Wilkerson, J., Murdoch, N., Michel, P., Ramesh, K. T., et al. (2014). Thermal fatigue as the origin of regolith on small asteroids. *Nature*, *508*(7), 233–236. https://doi.org/10.1038/nature13153

DellaGiustina, D. N., Burke, K. N., Walsh, K. J., Smith, P. H., Golish, D. R., Bierhaus, E. B., et al. (2020). Variations in color and reflectance on the surface of asteroid (101955) Bennu. *Science*, *370*(6517), 674. https://doi.org/10.1126/science.abc3660

DellaGiustina, D. N., Kaplan, H. H., Simon, A. A., Bottke, W. F., Avdellidou, C., Delbo, M., et al. (2021). Exogenic basalt on asteroid (101955) Bennu. *Nature Astronomy*, *5*(1), 31–38. https://doi.org/10.1038/s41550-020-1195-z

Dombard, A. J., Barnouin, O. S., Prockter, L. M., & Thomas, P. C. (2010). Boulders and ponds on the Asteroid 433 Eros. *Icarus*, *210*(2), 713–721. https://doi.org/10.1016/j.icarus.2010.07.006

Ebihara, T., Yumoto, K., Sugita, S., Honda, R., Kameda, S., Tatsumi, E., et al. (2021). Investigation of distribution and orientations of boulders on asteroid Ryugu: Implications for surface evolution. In *Lunar and Planetary Science Conference* (Vol. 2548, p. 1902).

GDR MiDi. (2004). On dense granular flows. *The European Physical Journal E*, *14*(4), 341–365. https://doi.org/10.1140/epje/i2003-10153-0

Golish, D. R., Drouet d'Aubigny, C., Rizk, B., DellaGiustina, D. N., Smith, P. H., Becker, K., et al. (2020). Ground and in-flight calibration of the OSIRIS-REx Camera Suite. *Space Science Reviews*, *216*(1), 12. https://doi.org/10.1007/s11214-019-0626-6

Hamilton, V. E., Simon, A. A., Christensen, P. R., Reuter, D. C., Clark, B. E., Barucci, M. A., et al. (2019). Evidence for widespread hydrated minerals on asteroid (101955) Bennu. *Nature Astronomy*, *3*(4), 332–340. https://doi.org/10.1038/s41550-019-0722-2

Hartzell, C. M. (2019). Dynamics of 2D electrostatic dust levitation at asteroids. *Icarus*, *333*, 234–242. https://doi.org/10.1016/j.icarus.2019.05.013

Hergenrother, C. W., Adam, C. D., Chesley, S. R., & Lauretta, D. S. (2020). Introduction to the special issue: Exploration of the activity of asteroid (101955) Bennu. *Journal Of Geophysical Research: Planets*, *125*(9), e2020JE006549. https://doi.org/10.1029/2020JE006549

Hergenrother, C. W., Maleszewski, C. K., Nolan, M. C., Li, J. Y., d'Aubigny, C. Y. D., Shelly, F. C., et al. (2019). The operational environment and rotational acceleration of asteroid (101955) Bennu from OSIRIS-REx observations. *Nature Communications*, *10*(1), 1291. https://doi.org/10.1038/s41467-019-09213-x

Iverson, R. M. (1997). The physics of debris flows. *Reviews of Geophysics*, *35*(3), 245–296. https://doi.org/10.1029/97RG00426

Iverson, R. M., Reid, M. E., & LaHusen, R. G. (1997). Debris-flow mobilization from landslides 1. *Annual Review of Earth and Planetary Sciences*, *25*(1), 85–138. https://doi.org/10.1146/annurev.earth.25.1.85

Jawin, E. R., McCoy, T. J., Walsh, K. J., Connolly, H. C., Ballouz, R. L., Ryan, A. J., et al. (2022). Global geologic map of asteroid (101955) Bennu indicates heterogeneous resurfacing in the past 500,000 years. *Icarus*, 114992. https://doi.org/10.1016/j.icarus.2022.114992

Jawin, E. R., Walsh, K. J., Barnouin, O. S., McCoy, T. J., Ballouz, R. L., DellaGiustina, D. N., et al. (2020). Global patterns of recent mass movement on asteroid (101955) Bennu. *Journal of Geophysical Research: Planets*, *125*(9). https://doi.org/10.1029/2020JE006475

Kitazato, K., Milliken, R. E., Iwata, T., Abe, M., Ohtake, M., Matsuura, S., et al. (2019). The surface composition of asteroid 162173 Ryugu from Hayabusa2 near-infrared spectroscopy. *Science*, *364*(6437), 272–275. https://doi.org/10.1126/science.aav7432

Lauretta, D. S., DellaGiustina, D. N., Golish, D. R., Golish, D. R., Barnouin, O. S., Bottke, W. F., et al. (2019). The unexpected surface of asteroid (101955) Bennu. *Nature*, *568*(7750), 1–16. https://doi.org/10.1038/s41586-019-1033-6

Lauretta, D. S., Hergenrother, C. W., Chesley, S. R., Leonard, J. M., Pelgrift, J. Y., Adam, C. D., et al. (2019). Episodes of particle ejection from the surface of the active asteroid (101955) Bennu. *Science*, *366*(6470). https://doi.org/10.1126/science.aay3544

Marchi, S., Chapman, C. R., Barnouin, O. S., Richardson, J. E., & Vincent, J. B. (2015). Cratering on asteroids. *Asteroids IV* (pp. 725–744). https://doi.org/10.2458/azu_uapress_9780816532131-ch037

Michikami, T., & Hagermann, A. (2021). Boulder sizes and shapes on asteroids: A comparative study of Eros, Itokawa and Ryugu. *Icarus*, *357*, 114282. https://doi.org/10.1016/j.icarus.2020.114282

Molaro, J. L., Walsh, K. J., Jawin, E. R., Ballouz, R. L., Bennett, C. A., DellaGiustina, D. N., et al. (2020). In situ evidence of thermally induced rock breakdown widespread on Bennu's surface. *Nature Communications*, 1–11. https://doi.org/10.1038/s41467-020-16528-7

Nolan, M. C., Howell, E. S., Scheeres, D. J., McMahon, J. W., Golubov, O., Hergenrother, C. W., et al. (2019). Detection of rotational acceleration of Bennu using HST light curve observations. *Geophysical Research Letters*, *46*(4), 1956–1962. https://doi.org/10.1029/2018GL080658

Perry, M., Barnouin, O., Daly, R., Bierhaus, E., Ballouz, R.-L., Walsh, K., et al. (2022). Impact-crater ejecta on Bennu indicate a surface with very low strength. *Nature Geoscience*. https://doi.org/10.1038/s41561-022-00937-y

Quaide, W. L., & Oberbeck, V. R. (1968). Thickness determinations of the lunar surface layer from lunar impact craters. *Journal of Geophysical Research*, *73*(16), 5247–5270. https://doi.org/10.1029/JB073i016p05247

Richardson, D. (2000). Direct large-scale N-body simulations of planetesimal dynamics. *Icarus*, *143*(1), 45–59. https://doi.org/10.1006/icar.1999.6243

Richardson, J. E., Melosh, H. J., Greenberg, R. J., & O'Brien, D. P. (2005). The global effects of impact-induced seismic activity on fractured asteroid surface morphology. *Icarus*, *179*(2), 325–349. https://doi.org/10.1016/j.icarus.2005.07.005

Rizk, B., Drouet d'Aubigny, C., Golish, D., DellaGiustina, D., & Lauretta, D. (2019). *Origins, Spectral Interpretation, Resource Identification, Security, Regolith Explorer (OSIRIS-REx): OSIRIS-REx Camera Suite (OCAMS) Bundle*. NASA Planetary Data System. Retrieved from https://arcnav.psi.edu/urn:nasa:pds:orex.ocams

Rizk, B., Drouet d'Aubigny, C., Golish, D., Fellows, C., Merrill, C., Smith, P., et al. (2018). OCAMS: The OSIRIS-REx camera suite. *Space Science Reviews*, *214*(1), 26–55. https://doi.org/10.1007/s11214-017-0460-7

Rizos, J., de León, J., Licandro, J., Golish, D., Campins, H., Tatsumi, E., et al. (2021). Bennu's global surface and two candidate sample sites characterized by spectral clustering of OSIRIS-REx multispectral images. *Icarus*, *364*, 114467. https://doi.org/10.1016/j.icarus.2021.114467

Roberts, J. H., Barnouin, O. S., Daly, M. G., Walsh, K. J., Nolan, M. C., Daly, R. T., et al. (2021). Rotational states and shapes of Ryugu and Bennu: Implications for interior structure and strength. *Planetary and Space Science*, *204*, 105268. https://doi.org/10.1016/j.pss.2021.105268

Rubincam, D. P. (2000). Radiative spin-up and spin-down of small asteroids. *Icarus*, *148*(1), 2–11. https://doi.org/10.1006/icar.2000.6485

Scheeres, D. J., Hesar, S. G., Tardivel, S., Hirabayashi, M., Farnocchia, D., McMahon, J. W., et al. (2016). The geophysical environment of Bennu. *Icarus*, *276*, 116–140. https://doi.org/10.1016/j.icarus.2016.04.013

Scheeres, D. J., McMahon, J. W., French, A. S., Brack, D. N., Chesley, S. R., Farnocchia, D., et al. (2019). The dynamic geophysical environment of (101955) Bennu based on OSIRIS-REx measurements. *Nature Astronomy*, *3*(4), 352–361. https://doi.org/10.1038/s41550-019-0721-3

Schwan, J., Wang, X., Hsu, H. W., Grün, E., & Horanyi, M. (2017). The charge state of electrostatically transported dust on regolith surfaces. *Geophysical Research Letters*, *44*(7), 3059–3065. https://doi.org/10.1002/2017GL072909

Schwartz, S. R., Ballouz, R. L., Asphaug, E. I., Barnouin, O. S., Bennett, C., Burke, K. N., et al. (2019). What can the orientations of Bennu's boulders tell us about its evolution? In *Paper presented at 50th Annual Lunar and Planetary Science Conference* (Vol. 2132, p. 2595).

Schwartz, S. R., Richardson, D. C., & Michel, P. (2012). An implementation of the soft-sphere discrete element method in a high-performance parallel gravity tree-code. *Granular Matter*, *14*(3), 363–380. https://doi.org/10.1007/s10035-012-0346-z

Seabrook, J. A., Daly, M. G., Barnouin, O. S., Johnson, C. L., Nair, A. H., Bierhaus, E. B., et al. (2019). Global shape modeling using the OSIRIS-REx scanning Laser Altimeter. *Planetary and Space Science*, *177*, 104688. https://doi.org/10.1016/j.pss.2019.07.003

Stadel, J. G. (2001). *Cosmological N-body simulations and their analysis* (PhD Thesis, pp. 1–141). University of Washington.

Sugita, S., Honda, R., Morota, T., Kameda, S., Sawada, H., Tatsumi, E., et al. (2019). The geomorphology, color, and thermal properties of Ryugu: Implications for parent-body processes. *Science*, *364*(6437). eaaw0422. https://doi.org/10.1126/science.aaw0422

Thomas, P. C., Prockter, L., Robinson, M., Joseph, J., & Veverka, J. (2002). Global structure of asteroid 433 Eros. *Geophysical Research Letters*, *29*(10), 46–41. https://doi.org/10.1029/2001GL014599

Thuillet, F., Michel, P., Maurel, C., Ballouz, R.-L., Zhang, Y., Richardson, D. C., et al. (2018). Numerical modeling of lander interaction with a low-gravity asteroid regolith surface. *Astronomy & Astrophysics*, *615*, A41. https://doi.org/10.1051/0004-6361/201832779

Tsuchiyama, A., Uesugi, M., Matsushima, T., Michikami, T., Kadono, T., Nakamura, T., et al. (2011). Three-dimensional structure of Hayabusa samples: Origin and evolution of Itokawa regolith. *Science*, *333*(6), 1125–1128. https://doi.org/10.1126/science.1207807

Walsh, K. J., Connolly, H. C., McCoy, T. J., Delbo, M., Pajola, M., Schwartz, S. R., et al. (2019). Craters, boulders and regolith of (101955) Bennu indicative of an old and dynamic surface. *Nature Geoscience*, *12*(4), 242–246. https://doi.org/10.1038/s41561-019-0326-6

Walsh, K. J., Richardson, D. C., & Michel, P. (2008). Rotational breakup as the origin of small binary asteroids. *Nature*, *454*(7), 188–191. https://doi.org/10.1038/nature07078

Zhang, Y., Richardson, D. C., Barnouin, O. S., Maurel, C., Michel, P., Schwartz, S. R., et al. (2017). Creep stability of the proposed AIDA mission target 65803 Didymos: I. Discrete cohesionless granular physics model. *Icarus*, *294*, 98–123. https://doi.org/10.1016/j.icarus.2017.04.027

Zhang, Y., Richardson, D. C., Barnouin, O. S., Michel, P., Schwartz, S. R., & Ballouz, R.-L. (2018). Rotational failure of rubble-pile bodies: Influences of shear and cohesive strengths. *The Astrophysical Journal*, *857*(1), 15. https://doi.org/10.3847/1538-4357/aab5b2